Scanning Microscopy Vol. 11, 1997 (Pages 301-322) 0891-7035/97$5.00+.25
Scanning Microscopy International, Chicago (AMF O'Hare), IL 60666 USA

CHALLENGES OF THREE-DIMENSIONAL RECONSTRUCTION OF RIBONUCLEOPROTEIN COMPLEXES FROM ELECTRON SPECTROSCOPIC IMAGES: RECONSTRUCTING RIBOSOMAL RNA

D.R. Beniac[1], G.J. Czarnota[2], T.A. Bartlett[1], B.L. Rutherford[2], F.P. Ottensmeyer[2] and G. Harauz[1]*
[1]Molecular Biology and Genetics, and Biophysics Interdisciplinary Group, University of Guelph, Guelph, Ontario, and [2]Molecular and Structural Biology, Ontario Cancer Institute, and Department of Medical Biophysics, University of Toronto, Ontario, Canada

Abstract

Quantitative image analysis of electron spectroscopic images of *Escherichia coli* and *Thermomyces lanuginosus* ribosomal subunits has presented unique challenges and has resulted in new algorithmic developments generally applicable to dark-field and electron spectroscopic images of biological macromolecules and their complexes. These improvements include a neighbourhood growing pretreatment procedure to delineate the boundary of the two-dimensional structure, the use of mutual correlation functions rather than cross-correlation functions to reduce the effects of low spatial frequency components, and angular determination using iterative quaternion-assisted angular reconstitution to compute a three-dimensional reconstruction. These investigations have produced direct information regarding ribosomal RNA (rRNA) architecture in the large and small ribosomal subunits of prokaryotic and eukaryotic organisms.

Key Words: Ribosomes, electron spectroscopic imaging, ribosomal RNA, quaternions, three-dimensional reconstruction, image analysis.

*Address for correspondence:
George Harauz
Molecular Biology and Genetics,
University of Guelph,
Guelph, Ontario, Canada, N1G 2W1
Telephone number: (519) 824-4120, (ext. 2535)
FAX number: (519) 837-2075
E-mail: gharauz@uoguelph.ca

Introduction

Ribosomal RNA (rRNA) has central importance in the architecture of the ribosome complex and in protein synthesis (Moore, 1988; Brimacombe, 1995; Mueller *et al*., 1995). The different rRNA species and subunits are usually denoted by their predominant sedimentation coefficients: 16S in the prokaryotic small (30S) ribosomal subunit, 5S and 23S in the prokaryotic large (50S) ribosomal subunit, 18S in the eukaryotic small (40S) ribosomal subunit, and 5S, 5.8S, and 28S in the eukaryotic large (60S) ribosomal subunit, where S is the "Svedberg" coefficient. Every biochemical and biophysical approach extant has been used to probe the structures of the ribosomal complexes and the organisation of rRNA within them, but of most relevance to us here are computational electron image analysis and reconstruction (Frank, 1992, 1996). Science does not progress simply by new ideas, but also by new techniques. Significantly, the ribosome nut has inspired the creation of new tools to help crack it. We note especially the sophisticated pattern analysis algorithms created in the framework of "single particle electron crystallography" (Frank, 1996). In this paper, we first review transmission electron microscopy (TEM) approaches to probing the tertiary structure of rRNA *in situ*, and then describe in detail our own work using electron spectroscopic imaging (ESI) (Beniac and Harauz, 1993, 1995a; Beniac *et al*., 1997a,b) to study rRNA in a prokaryote (the commonly studied eubacterium *Escherichia coli*) and in a eukaryote (the mildly thermophilic fungus *Thermomyces lanuginosus*).

Electron microscopy of ribosomal RNA in intact ribosomes

Well over a decade ago, the group of Professor Hoppe at the Max-Planck-Institut für Biochemie in Martinsried, Germany, reconstructed individual *E. coli* 30S and 50S ribosomal subunits from tomographic tilt series (Knauer *et al*., 1983; Oettl *et al*., 1983). The complexes were negatively stained by embedding in uranyl acetate, and regions of high density in the reconstruction were postulated to represent rRNA that had been *positively* stained (Fig. 1). This work is of historical interest because it challenged the microscopical and computational capabilities of the time. In another

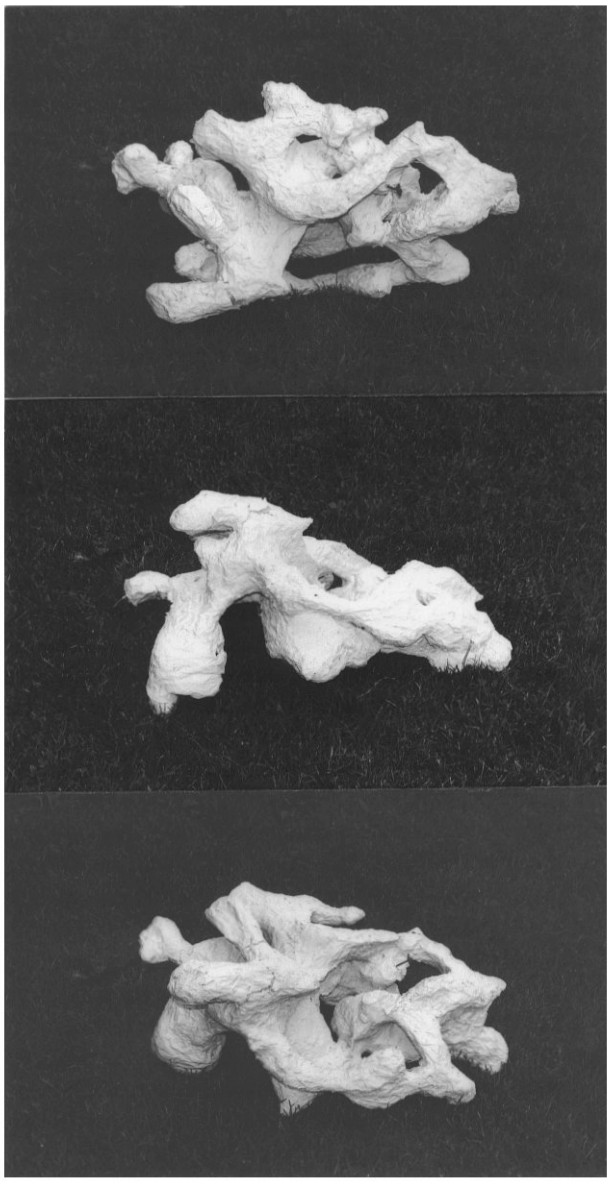

Figure 1. Plaster model representing an interpretation of the path of *E. coli* 16S rRNA in the reconstructions of 30S subunits from tilt series (Knauer *et al*., 1983). (This landmark of electron microscopical achievement now decorates the tea room of the Molekulare Strukturbiologie group at the Max-Planck-Institut für Biochemie, Martinsried, Germany.)

approach, Kühlbrandt and Unwin (1982) applied contrast variation to distinguish the rRNA from the protein within crystalline ribosomes from lizard oocytes. Using media of variable electron scattering density to match out the contribution to image contrast of protein or nucleic acid, it was found that the rRNA formed a dense central core with extensions to the surface, especially in the region of the subunit interface. Elsewhere, the dedicated scanning transmission electron microscope (STEM) at Brookhaven National Laboratories was used to differentiate between signals from scattered electrons at large and small angles, enabling the approximate mapping of the distribution of the phosphate backbone of the rRNA *in situ* in the *E. coli* ribosomal subunits (Boublik *et al*., 1990; Boublik and Wall, 1992). Immunoelectron microscopy has been invaluable in localising specific rRNA sequence segments (e.g., Stöffler-Meilicke *et al*., 1981; McWilliams and Glitz, 1991).

Cryoelectron microscopy has provided the best information on ribosomal structure, and the Albany group has been the vanguard of this discipline. Specifically addressing the question of rRNA organisation, Frank and coworkers (Frank *et al*., 1991) performed a three-dimensional (3D) reconstruction of the 70S *E. coli* ribosome encased in vitreous ice. Quantitative manipulation of the reconstruction by density discrimination yielded a structure interpretable as being ribosomal RNA, with an intriguing potential rRNA junction at the subunit interface. Most recently, the Albany and Berlin groups working independently achieved high resolution reconstructions of *E. coli* 70S ribosomes embedded in vitreous ice, and these studies have set the gold standard for the field (Frank and Penczek, 1995; Frank *et al*., 1995a,b; Stark *et al*., 1995). During the gestation of this present manuscript, further reconstructions from the Albany group were published (Agrawal *et al*., 1996; Lata *et al*., 1996; Verschoor *et al*., 1996). It is difficult to envision that techniques other than cryoelectron microscopy might still be worthwhile to pursue in ribosomology.

Electron spectroscopic imaging

Nonetheless, it still can help to look at biological macromolecules in a different way. Dark field electron microscopy (EM) and ESI (Ottensmeyer and Andrew, 1980; Ottensmeyer, 1982, 1984) are two different modes of imaging macromolecular complexes. ESI uses a standard TEM which is equipped with an energy filter below the objective lens (Ottensmeyer, 1984). By using only electrons which have lost a specific amount of energy due to specific inner-shell ionisation interactions with the specimen, it is possible to form an elemental map of the specimen. In nucleoprotein complexes, a map of the phosphorus distribution represents primarily a projection of the phosphate backbone of the nucleic acid component, since the amount of phosphorus in phosphorylated proteins is usually much smaller. Since ESI's inception, important structural and functional data have been gathered by the ability to visualise selectively to high resolution the nucleic acid components of nucleosomes, ribosomes, the signal recognition particle, the TFIIIA-5S rRNA complex, DNA, and sundry other protein-DNA complexes. In particular, the visualisation of rRNA *in situ* in the intact ribosomal subunit by ESI was demonstrated

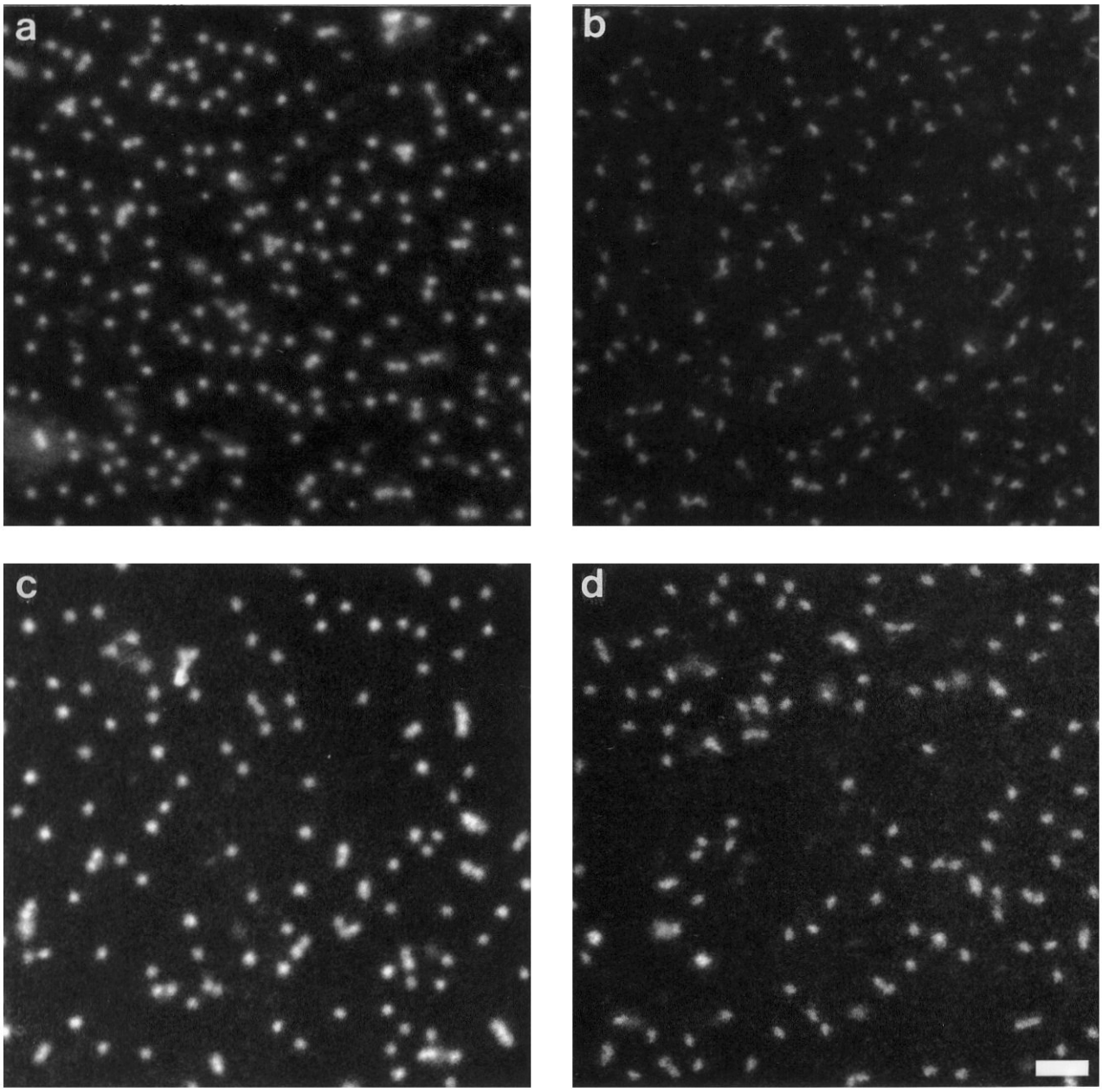

Figure 2. Areas of 150 eV loss electron spectroscopic images of (**a**) *E. coli* large and (**b**) *E. coli* small and (**c**) *Th. lanuginosus* large and (**d**) *Th. lanuginosus* small ribosomal subunits. These images have been printed directly from the negatives onto photographic paper. Contrast is thus reversed from that in the electron microscope film. Here, the ribosomes are white against a dark carbon film background. Bar = 100 nm.

as feasible, over a decade ago (Korn *et al*., 1983; Boublik *et al*., 1984). Unfortunately, these results have never been fully accepted by the scientific community, mainly because of the unavoidably high radiation doses inherent in the technique, measurements of which were published by Bazett-Jones *et al*. (1988). Electron spectroscopic imaging is a **microanalytical** technique, not just an imaging one. The higher irradiation demands of the technique are for localising and identifying the phosphorus signal.

Electron spectroscopic imaging can be a useful and **complementary** technique to vitreous ice imaging of nucleoprotein complexes. In principle, the most obvious advantages of ESI to the study of ribosome structure are a potential resolution of 0.3-0.5 nm of unstained specimens,

with a minimum detectable mass of 20 to 50 atoms of phosphorus (Adamson-Sharpe and Ottensmeyer, 1981; Bazett-Jones and Ottensmeyer, 1981; Bazett-Jones, 1993). Over many recent years, we have been applying quantitative image analysis to ES images of ribosomal subunits (Beniac and Harauz, 1993, 1995a; Beniac *et al.*, 1997a,b). At the time that we initiated these studies, *circa* 1989, the previously demonstrated potential of ESI was singularly alluring. It was initially thought to be a straightforward matter to spread some purified ribosomes on a grid, image them electron spectroscopically, and obtain beautiful pictures by computational single particle analysis. In retrospect, this approach presented unique challenges, including subunit isolation, their preparation for electron microscopy, and the requirement for new algorithmic developments. We present here our acquired knowledge, especially in the latter discipline, as a rational framework generally applicable to dark-field and electron spectroscopic images of biological macromolecules and their complexes.

Materials and Methods

Isolation of ribosomal subunits

Escherichia coli [strain AB 264; American Type Culture Collection (ATCC), Rockville, MD] and *Thermomyces lanuginosus* (ATCC 16455) ribosomal subunits were isolated by sucrose density gradient centrifugation. All procedures were continuous from cell lysis to freeze-drying to ensure particle integrity. Under no circumstances were samples frozen between steps. The samples were constantly maintained at 4°C, and RNase and protein inhibitors were used to ensure that enzymatic degradation did not occur. After pooling of gradient fractions enriched in small or large ribosomal subunits, the sucrose was removed, and the salt concentration of the buffer was reduced by dialysis against a 1 liter volume of dialysis buffer for a 12 hour period with several buffer changes. Shortcuts here were definitely deleterious, with any remaining sucrose or salts forming disturbing menisci around the pure particles. *E. coli* ribosomal subunits were dialysed against 10 mM HEPES (N-[2-hydroxyethyl] piperazine-N'-[2-ethanesulfonic acid])-KOH (pH 7.4), 60 mM KCl, 10 mM 2-mercapto-ethanol, 2 mM $Mg(CH_3COO)_2 \cdot 4H_20$. *Th. lanuginosus* ribosomal subunits were dialysed against 10 mM HEPES-KOH (pH 7.5), 0.9 M KCl, 10 mM 2-mercapto-ethanol, 12 mM $Mg(CH_3COO)_2 \cdot 4H_20$.

Preparation for electron microscopy

Ultrathin carbon film (~5-6 nm thick) was produced by indirect evaporation onto mica, scored and floated off onto the surface of sterilised ddH_2O (distilled deionised water), and picked up with precleaned 1000 mesh copper or nickel grids. Both types of grids were used to be able to freeze-dry two different specimens at the same time. The coated grids were wicked dry, and allowed to stand for a 12 hour period to allow the carbon to adhere firmly to the support. Omission of this 12 hour drying step resulted in the carbon film detaching from the support grid in the subsequent liquid propane plunging step. A 25 µl drop of the dialysed ribosomal subunit enriched sample (adjusted to an A_{260}/ml of 0.2) was applied to the carbon film side of a carbon film - 1000 mesh grid. The sample was allowed to adsorb to the carbon film for 60 seconds, and the excess sample was removed by wicking with filter paper; this step was followed instantly by application of a 25 µl droplet of sterile ddH_2O to rinse the sample. This wicking-washing procedure was repeated several times to rinse the sample thoroughly. The grid with the sample was then held in a pair of reverse tension forceps, wicked almost dry, and immediately plunged into a bath of liquid propane suspended in a cup in a bath of liquid nitrogen (-196°C). The frozen sample was then transferred into a copper tray suspended in liquid nitrogen; the copper tray (with grids in it) was then transferred to a pre-cooled (-196°C) cryo-stage of a Balzers (Liechtenstein) 360 M freeze fracture unit. The grids were then transferred to the cryo-stage with pre-cooled forceps, the copper tray was removed, and the freeze etch unit was sealed. A high vacuum was then drawn (10^{-5} Torr), while the sample temperature was kept at -196°C. Over a half hour period, the sample was gradually warmed to -84°C; this step was followed by a 2 h drying period at -84°C. The sample was then gradually brought up to room temperature, removed from the Balzers freeze etcher, and stored under vacuum in a bell jar until viewed in the electron microscope.

Electron spectroscopic imaging

Electron spectroscopic imaging was performed in a Zeiss (Oberkochen, Germany) EM902 electron microscope equipped with a Castaing-Henry type energy filter, at a magnification of 30000x and at an accelerating voltage of 80 keV. The energy selecting slit was set at a width of 18 eV. Two micrographs were then taken of previously unilluminated regions of the specimen at 150 eV and 100 eV energy losses. The 100 eV image produced non-specific mass density images of the subunit, and the 150 eV image represented a phosphorus enhanced image of the sample superimposed over a non-specific mass density. The 150 eV image was recorded first because we considered it to be the more important one, i.e., a phosphorus enhanced image. We use the term "doublets" to refer to these pairs of images of the specimen recorded at different energy losses. Electron micrographs were visually examined, and those of best optical quality (focus, astigmatism, optical density within

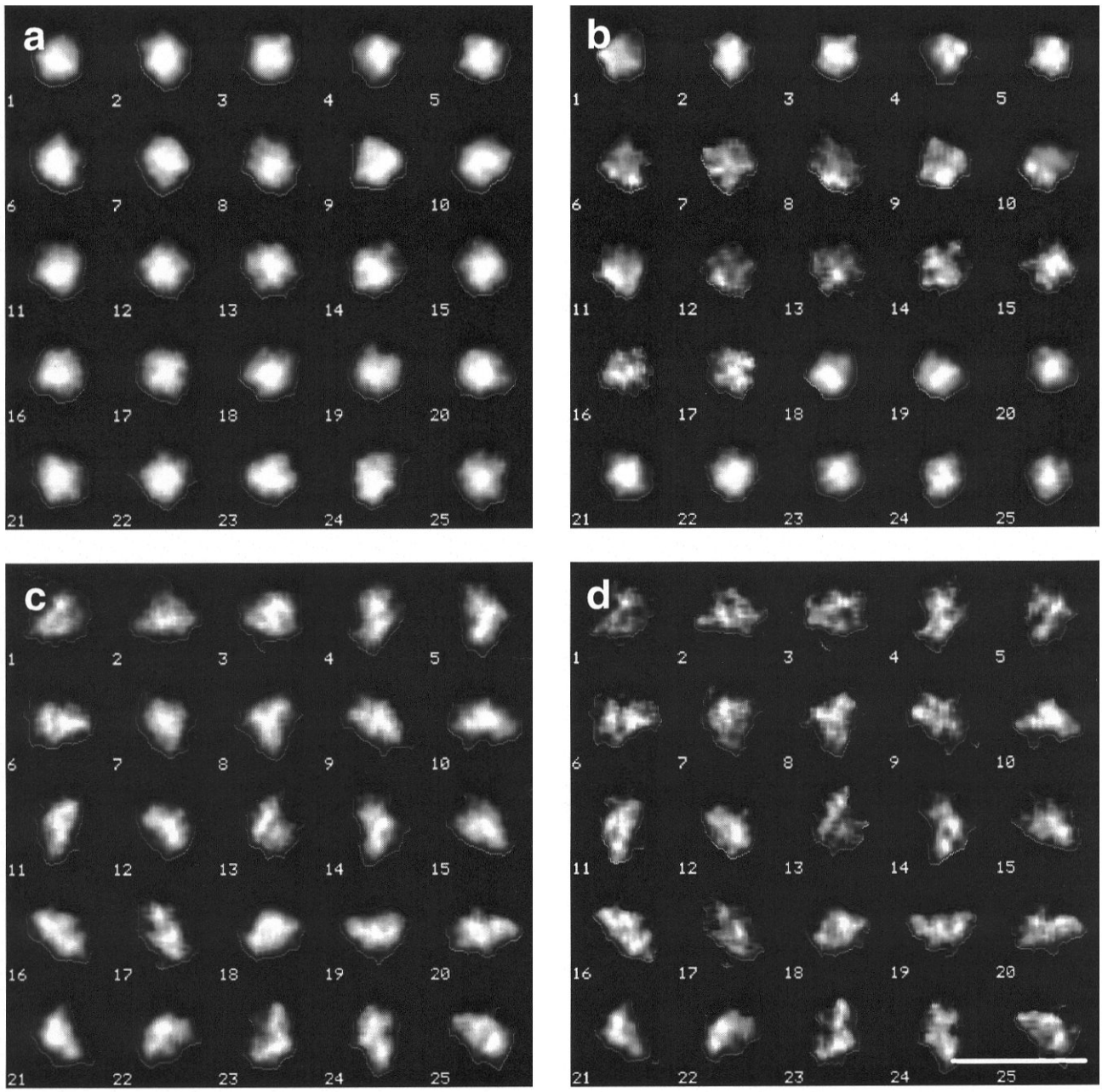

Figure 3. Galleries of 150 eV loss and corresponding NetP images of farrow-segmented (pretreated) single ribosomal particles. The farrow-segmentation process was applied to the 150 eV loss images; subsequently, the boundary of the pretreated 150 eV loss image was used to delineate the (same) particle in the NetP image. (**a**) *E. coli* large ribosomal subunits, farrow-segmented 150 eV loss images. (**b**) Corresponding *E. coli* large ribosomal subunits, farrow-segmented NetP images. (**c**) *E. coli* small ribosomal subunits, farrow-segmented 150 eV loss images. (**d**) Corresponding *E. coli* small ribosomal subunits, farrow-segmented NetP images. Bar = 50 nm.

the linear response range of the emulsion) were chosen for subsequent analysis (Fig. 2). Electron micrographs were digitised using an Optronics (Chelmsford, MA) rotating drum densitometer; a 1200 x 1200 pixel area was acquired using a 25 μm aperture, with a corresponding scanning step size of 25 μm. During digitisation, the emulsion of the negative was kept facing into the drum to preserve handedness in the images. All micrographs were mounted so that doublet images (i.e., at 150 and 100 eV loss) would be scanned over the same central region of the micrograph to facilitate

computer alignment of doublet members. Digitisation was restricted to the center of the micrograph to maintain the same energy loss range from image to image.

Digitised images were then transferred to an IBM (Markham, Ont., Canada) RISC System/6000 PowerStation 220 for analysis within the framework of the IMAGIC-V system (van Heel *et al*., 1996). The digitised ES images were pretreated with a 3x3 pixel median filter to suppress some of the image noise, followed by interactively selecting matching ribosomal subunits within each image, using a mouse and cursor. The centers of mass of the 200 or so matching ribosomal subunits were used as fiducial points to calculate the rotation and translational shifts necessary in order to bring the paired images into register with one another. Individual small (904 for *Th. lanuginosus* and 927 for *E. coli*) and large (789 for *Th. lanuginosus* and 1105 for *E. coli*) ribosomal subunits were then interactively selected, i.e., subimages of size 64x64 pixels containing a single ribosomal subunit centered within them were selected from the larger 150 eV and 100 eV loss images.

The first step in producing the net phosphorus (NetP) image from the doublet of each particle was the removal of the background density due to the photographic emulsion by subtraction of the average density measured from a corner of the negative. Next, the extrapolation of the energy loss spectrum under the ionisation edge was calculated using the relationship $I = AE^{-R}$, where I is the intensity, E is the energy loss, and A and R are constants. In a so-called two parameter fit, the values of A and R are calculated for each point in the image, and two reference images (below the ionisation edge) are required (Ottensmeyer, 1986a,b; Bazett-Jones *et al*., 1988; Bazett-Jones, 1993). Here, we used a one parameter fit with a value of R constant over the whole image and only A varying, since only one reference image was taken **deliberately to limit the cumulative electron dose**. The net phosphorus map was calculated by subtracting the extrapolated 100 eV loss image from the 150 eV loss image. Although the number of phosphorus atoms is only about 2.5% of the total number of carbon-like atoms, the inelastic scattering cross-section of phosphorus is about 15 times stronger than carbon at 150 eV (Ottensmeyer, 1986a,b; Egerton, 1988; Heng *et al*., 1990) and so a large NetP signal is realised (Bazett-Jones, 1993; Bazett-Jones and Ottensmeyer, 1981).

For a strong NetP signal such as from a ribosome, which constitutes about 20-30% of the background signal (cf., Heng *et al*., 1990), the one-parameter approximation would introduce a systematic error of no more than 15% while reducing the random error by 40% compared to the two-parameter fit. Obviously, for smaller elemental concentrations, more complex three or four window methods are required. The integrated optical densities over corresponding background areas comprising only carbon film were used to determine multiplicative factors to correct for the slightly unequal exposures of each doublet member. We determined empirically that more satisfactory NetP images were obtained by performing the above calculation for each particle separately, using the **adjacent** carbon film density to compute background correction factors, rather than doing the calculation over a large area using an average carbon film density.

Two-dimensional electron image analysis

Because of computer resource limitations, each of the four data sets (*Th. lanuginosus* and *E. coli* large and small ribosomal subunits) was further reduced to 300 particles and treated separately. The particles were chosen solely on the basis of their structural integrity and isolation from other complexes which might interfere with the analysis. Since the 150 eV loss images contained stronger and more distinctive signals than the corresponding 100 eV loss ones, and were inherently less noisy than the corresponding NetP maps, all sorting and alignment algorithms were applied to the first population. Once 150 eV loss images were aligned rotationally and translationally, and classified, the corresponding NetP images were moved and averaged using the same parameters. The aim of subsequent "single particle" image analysis was to sort these data into groups representing similar projections, for averaging to improve the signal-to-noise ratio and reproducible spatial resolution.

All images had already undergone a 3x3 pixel median filtering. A 2x2 zoom factor was then applied to each image to make each ribosomal subunit comprise a greater number of pixels within each image, to reduce subsequent interpolation errors due to effects of digitisation at a given pixel size. The subsequent set of operations constitute a pretreatment procedure which we have baptised as "farrow-segmentation" after its originator (Farrow and Ottensmeyer, 1992, 1993). First, the pixel of maximum intensity was determined in the center quarter of each image. Starting from this point, neighbouring pixels were marked, and a contiguous region was thus "grown" outwards until the integrated intensity of all pixels within the neighbourhood were a specified fraction (here, 1/3) of the integrated intensity of all pixels within the entire image. This operation served to distinguish the particle from its surrounding background which represented only carbon film. Previously, we had used objective thresholding algorithms focussed on discriminating "object" from "background" on the basis of grey level distributions (Beniac and Harauz, 1995b). The advantage of farrow-segmentation was the definition of a contiguous image region representing only the particle of interest.

After farrow-segmentation, all pixels outside the particle neighbourhood were set to a value of zero, and the value of the smallest positive gray level less 1 was then subtracted from the particle pixels. This way, the average

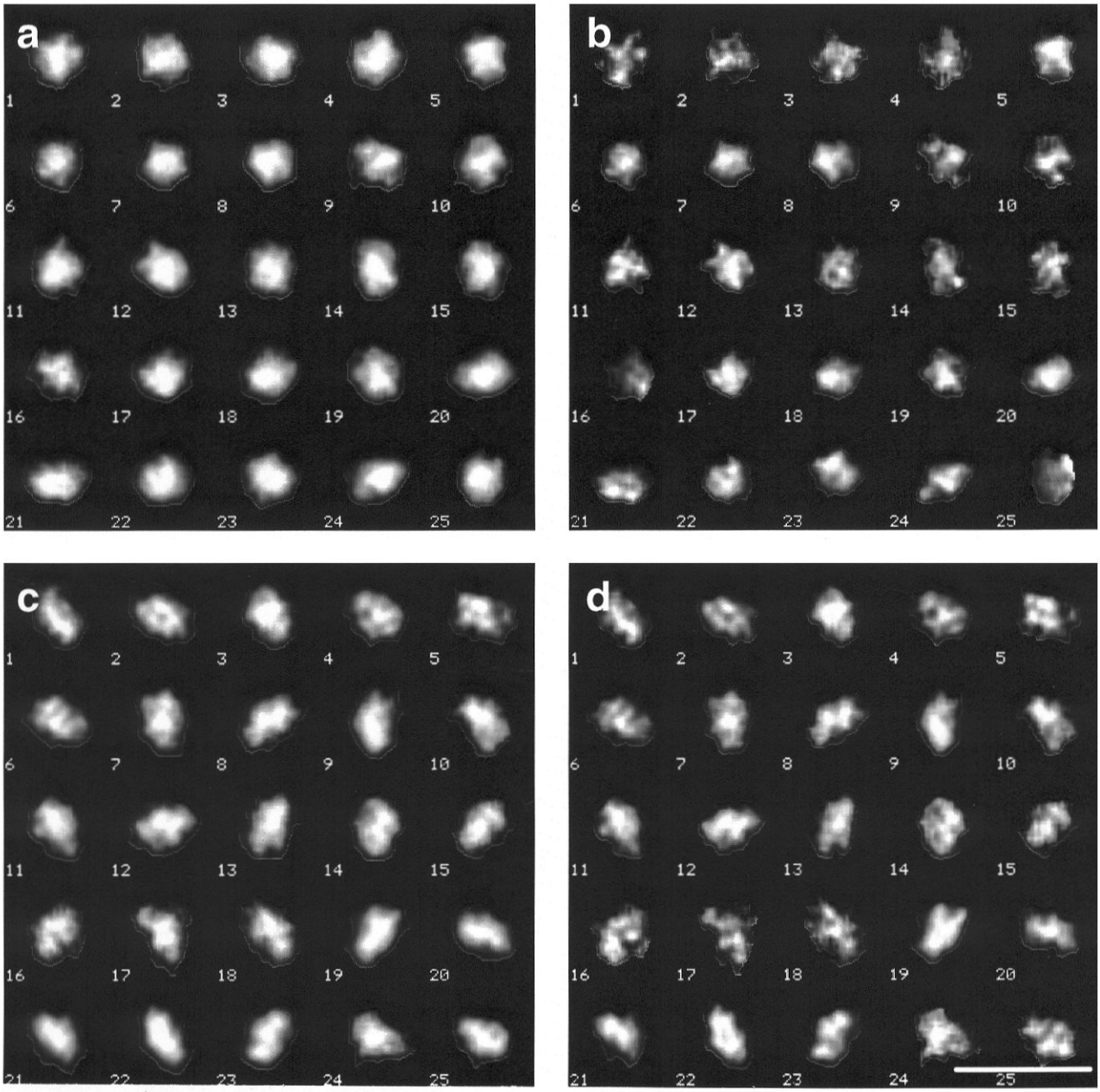

Figure 4. Galleries of 150 eV loss and corresponding NetP images of farrow-segmented (pretreated) single ribosomal particles. The farrow segmentation process was applied to the 150 eV loss images; subsequently, the boundary of the pretreated 150 eV loss image was used to bound the particle in the NetP image. (**a**) *Th. lanuginosus* large ribosomal subunits, farrow-segmented 150 eV loss images. (**b**) Corresponding *Th. lanuginosus* large ribosomal subunits, farrow-segmented NetP images. (**c**) *Th. lanuginosus* small ribosomal subunits, farrow-segmented 150 eV loss images. (**d**) Corresponding *Th. lanuginosus* small subunits, farrow-segmented NetP images. Bar = 50 nm.

(in the vicinity of the particle) density contribution of the carbon film was removed from the analysis. Then, all non-zero positive density values were normalised over the entire image population, being multiplied by a positive factor so that each particle had the same total intensity. By normalising all the images in this way, intensity differences were suppressed, enabling a better comparison of different images to one another. A translational alignment was performed last to match the center of mass of the particle with the geometric center of the image (Figs. 3 and 4). Then,

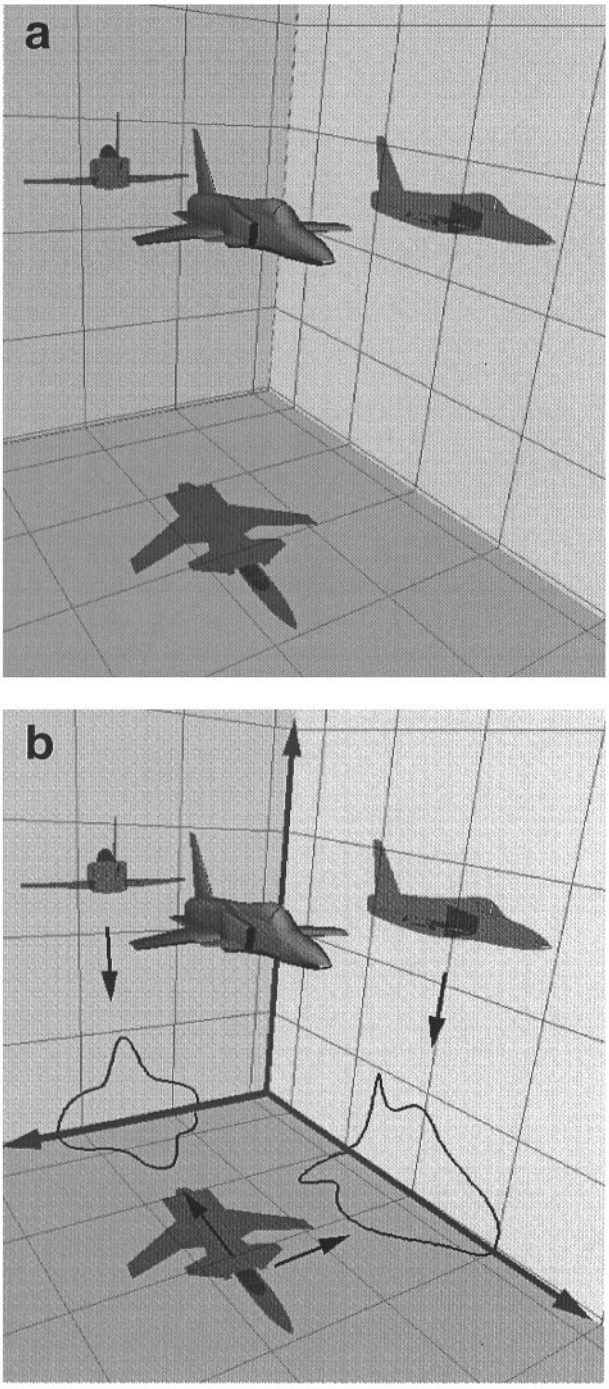

Figure 5 (*at left*). The essence of IQAD (Farrow and Ottensmeyer, 1992, 1993). A three-dimensional object viewed from different orientations presents different two-dimensional views. The shadows in (**a**) illustrate this first point. In real space, the 3D object is related mathematically to its 2D projections by line integration of the 3D density. In reciprocal (Fourier) space, the corresponding 3D and 2D Fourier transforms share common lines. The outlines in (**b**) are drawn to appertain to this second point. Three *different* 2D projections are necessary and sufficient to determine the Eulerian angles of rotation relating them. This general process is termed "angular reconstitution." The acronym IQAD was first used but is perhaps no longer adequate: it could mean either "iterative quaternionic angle determination" (GH), or "iterative quaternion-assisted angular reconstitution" (GJC). Both terms are equivalent.

each data set underwent at least 2 cycles of multi-reference alignment, multivariate statistical decomposition into principal components of variation, hierarchical ascendant classification, and interpretation and refinement of class averages (Frank, 1996). Another important difference here, however, is that mutual correlation functions rather than cross-correlation functions were used to reduce the effect of low spatial frequency components especially prevalent in such images (van Heel *et al*., 1992).

Three-dimensional reconstruction of ES images

The problem of determining the relative orientations of non-crystalline randomly oriented biological macromolecules has been a long-standing one. Here, we used a quaternion-assisted approach of angular reconstitution (Fig. 5) (Farrow and Ottensmeyer, 1992, 1993). This method exploits sinograms and sinogram correlation functions (Fig. 6) and the Central Axis (or Projection) Theorem to determine the relative angular orientations of the ribosomal subunits from their farrow-segmented 150 eV loss images. This theorem states that projection images of a particular macromolecule at different orientations share common lines of integrated intensity. By determining these common lines, it is possible to determine the relative angular orientations amongst many projection images. The initial orientation angles of the reconstructions were refined iteratively by a quaternion vector approach as described previously by Farrow and Ottensmeyer (1992, 1993). The method is robust, has been tested exhaustively with simulated images, and applied recently to structure determination of numerous proteins and nucleoproteins (e.g., Czarnota *et al*., 1994; Czarnota and Ottensmeyer, 1996; Bazett-Jones *et al*., 1996; Beniac *et al*., 1997b,c; Ridsdale *et al*., 1997). Again, mutual correlation functions between sinograms were employed instead of cross-correlation functions. Reconstruction was performed using filtered back-projection with exact filters (Harauz and van Heel, 1986).

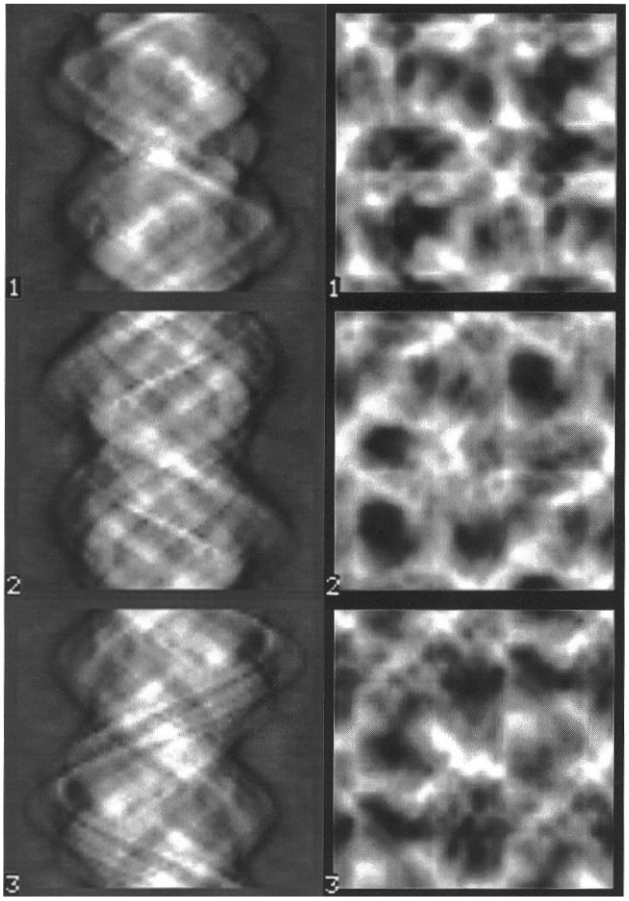

Figure 6. In real space angular reconstitution, sinograms and sinogram correlation functions (SCFs) must be calculated. On the left are 3 sinograms derived from 3 different 150 eV loss images of *E. coli* small ribosomal subunits. Each line in a sinogram represents a one-dimensional projection of the two-dimensional image at radial angles ranging uniformly from 0 (top line) to 2π (bottom line). On the left are the three sinogram correlation functions derived from pairs of sinograms: SCF 1 from sinograms 1 and 2; SCF 2 from sinograms 1 and 3; SCF 3 from sinograms 2 and 3. The value of each pixel in the SCF is the **mutual** correlation coefficient of a line in one sinogram with a line in another sinogram. The highest peak value in the SCF represents the orientation of the common line of one projection with another.

Results and Discussion

Electron spectroscopic imaging and digitisation

Sample preparation, imaging, and densitometry were performed after many trials. Many experiments with different buffers and different purification protocols were needed to obtain pure ribosomal subunit preparations, with minimal cross-contamination of large and small particles, and with minimal interference from buffers after freeze-drying.

The Zeiss EM902 is the first commercially available instrument capable of ESI with an in-column filter. Data were of necessity recorded on electron-sensitive film. This arrangement might sound archaic given the spate of technological developments, e.g., dedicated STEMs (Crewe, 1966) equipped with spectrometers (Engel and Reichelt, 1988; Haider, 1989; Engel and Colliex, 1993). However, film still remains a far more sensitive detector than some modern charge-coupled device (CCD) cameras (cf., de Bruijn *et al*., 1993; Beckers *et al*., 1994a,b, 1996). In the future, a dedicated STEM might be useful if equipped with an electron spectrometer and detector that counts single electrons rather than bunches of 30 for a single "event," and that reads signals on the fly rather than requiring 100 minutes for a simple image of 512x512 pixels. Finally, film densitometry required an accurate device - desktop scanners suitable for office publishing are simply too noisy. Here, the Optronics densitometer was one of the best that was available to us. Our use of a number of other densitometers had led at times to a loss of information due to an insufficient instrumental signal to noise ratio. Thus, the instrumentation used must be considered in comparing results, including negative ones, from different laboratories (de Bruijn *et al*., 1993; Beckers *et al*., 1994a,b, 1996).

Two-dimensional electron image analysis

In our previous studies (Beniac and Harauz, 1993, 1995a,b), we had lamented the difficulty of applying algorithms developed for single particle analysis of bright field images of negatively stained macromolecular preparations to dark field-like images of unstained samples. The former are horrible holograms (a term originating from Professor Kellenberger, quoted in Ottensmeyer, 1982); the latter are blobs (cf., reference to "blobology" on page 93 in McRee, 1993). In other words, the latter have a much higher relative component of low spatial frequency information and poorer intra-image definition of structural detail. Pretreatment of images by band-pass filtering, and alignment using cross-correlation functions, did not lend themselves to the facile production of homogeneous class averages that could be interpreted as corresponding to, say, the quasi-symmetric, crown, or skiff views so beautifully delineated in computational analyses of negatively stained preparations (van Heel and Stöffler-Meilicke, 1985); Harauz *et al*., 1987, 1988; Harauz, 1992; Harauz and Flannigan, 1992). As one potential solution to these problems, we experimented with orientationally invariant functions of moments of images of single ribosomal particles (Hawkes, 1980a,b; Teague, 1980; Beniac and Harauz, 1995b). We have

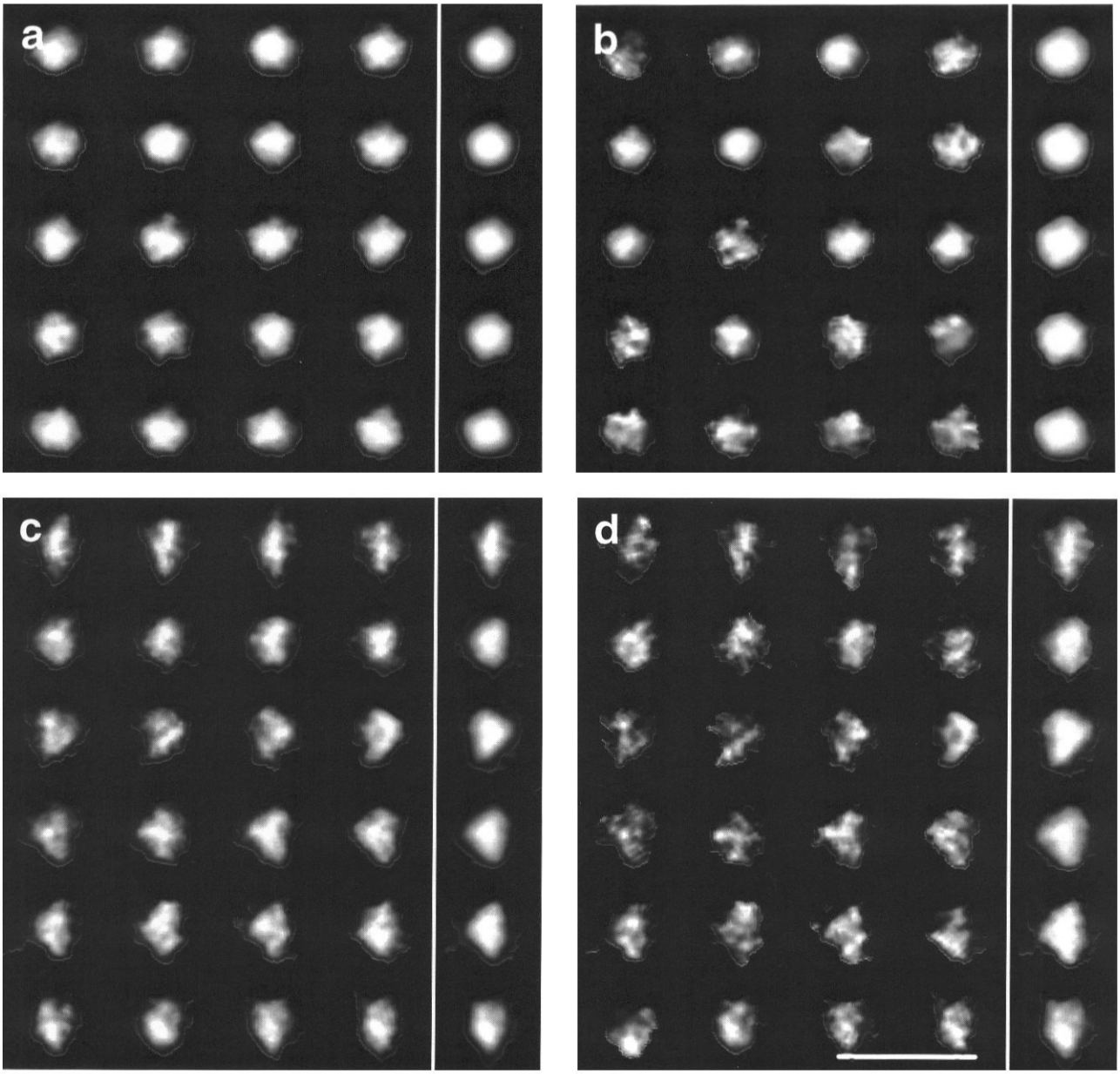

Figure 7. The compositions of classes derived by single particle analysis are illustrated here. Each row comprises five images of individual particles. The first four images are examples of farrow-segmented and aligned members of a particular class, whose average image is the 5th and last of that row. The 150 eV loss images are of *E. coli* 50S (**a**) and 30S (**c**) ribosomal subunits. The corresponding NetP images are of *E. coli* 50S (**b**) and 30S (**d**) ribosomal subunits.

not yet succeeded in developing this approach to the point where it can differentiate between subtly different orientations of macromolecules, although moment functions continue to be discussed considerably in the literature (Wallin and Kübler, 1995). Other kinds of orientation invariant functions of the macromolecular images also gave disappointing results in our hands (Schatz and van Heel, 1990, 1992).

However, we did identify the need for an objective differentiation of the particle from its carbon film background. In our earlier work, we used a variety of image thresholding algorithms (Beniac and Harauz, 1995a,b). Here, we used a neighbourhood-growing technique which had an advantage over simple thresholding of producing a more homogeneous set of particles in terms of areal size and total density. Subsequently, the use of **mutual** correlation

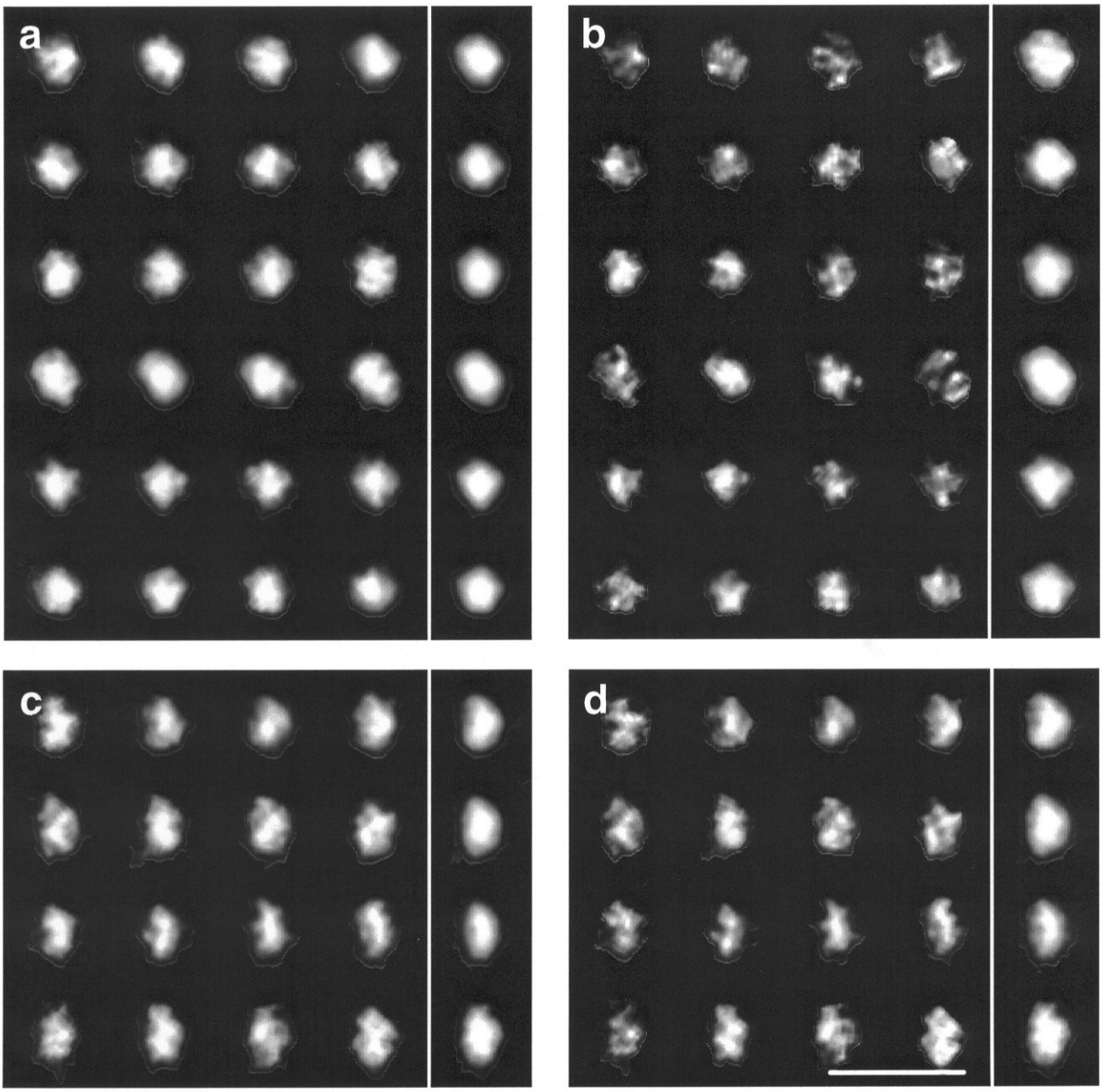

Figure 8. The compositions of classes derived by single particle analysis are illustrated here. Each row comprises five images of individual particles. The first four images are examples of farrow-segmented and aligned members of a particular class, whose average image is the 5th and last of that row. The 150 eV loss images are of *Th. lanuginosus* 60S (**a**) and 40S (**c**) ribosomal subunits. The corresponding NetP images are of *Th. lanuginosus* 60S (**b**) and 40S (**d**) ribosomal subunits.

functions, in which the Fourier transforms of images are divided by the square roots of their amplitudes at each point, led to better alignments (van Heel *et al*., 1992). The selection of multiple images as references for alignment ameliorated the problem of "reference bias" with satisfaction. Multivariate statistical analysis using χ^2 metrics (the canonical correspondence analysis) (Frank, 1996), hierarchical ascendant classification (Frank, 1996), and interactive subdivision of computer defined classes into smaller classes yielded homogeneous subgroups representing different particles lying in similar orientations in the plane (Figs. 7 and 8).

Are these results relevant biologically? After farrow-segmentation, it is evident that individual ribosomal

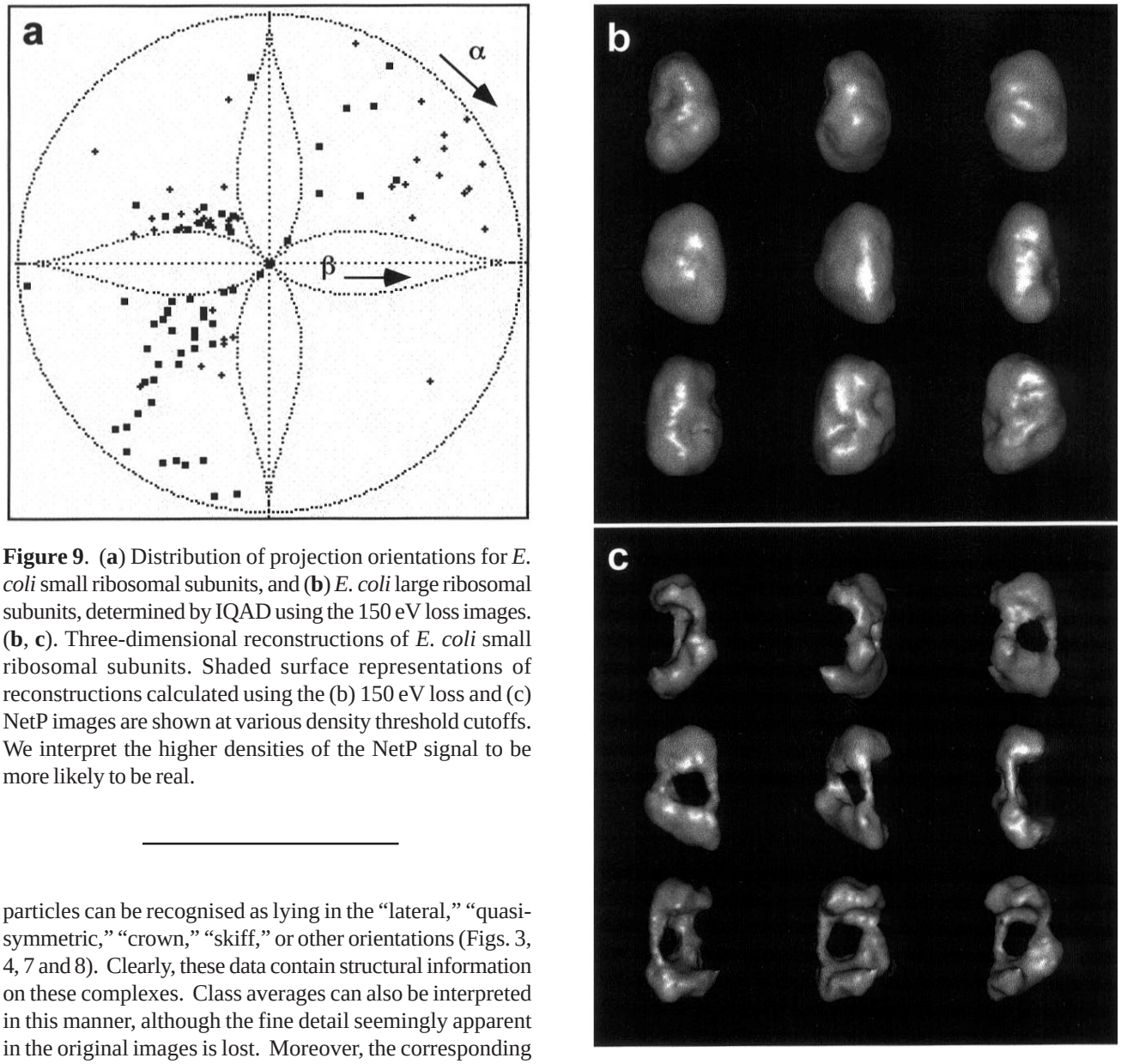

Figure 9. (**a**) Distribution of projection orientations for *E. coli* small ribosomal subunits, and (**b**) *E. coli* large ribosomal subunits, determined by IQAD using the 150 eV loss images. (**b**, **c**). Three-dimensional reconstructions of *E. coli* small ribosomal subunits. Shaded surface representations of reconstructions calculated using the (b) 150 eV loss and (c) NetP images are shown at various density threshold cutoffs. We interpret the higher densities of the NetP signal to be more likely to be real.

---

particles can be recognised as lying in the "lateral," "quasi-symmetric," "crown," "skiff," or other orientations (Figs. 3, 4, 7 and 8). Clearly, these data contain structural information on these complexes. Class averages can also be interpreted in this manner, although the fine detail seemingly apparent in the original images is lost. Moreover, the corresponding NetP class averages were equally blobby. What are the reasons for these disappointing results? First, structural variation due to preparation artefacts and radiation damage is one source of the severe blurring. Secondly, we hypothesise that the ribosomal subunits in these freeze-dried preparations present a **range** of orientations, including sig nificant "rocking" about the expected preferred ones such as the crown, etc. In negatively stained preparations, the intra image contrast afforded by stain penetration into the interior, as well as particle flattening caused by the preparation process (minimising the "rocking" effect), can fortuitously help make sensible the two-dimensional image sorting and averaging process. Here, however, such artefacts are not available to help us.

Clearly, we should resist overinterpreting the individual noisy electron spectroscopic images - we acknowledge that the particles have lost up to half of their mass during the microanalytical process. The ESI technique is always criticised on the basis of the high radiation dose that is inherently necessary to identify atomic elements. (As a microanalytical technique, it is nevertheless more dose-sparing than any other approach, often by at least an order of magnitude.) This criticism is one reason why we invoke image averaging as a means to "wash out" factors such as radiation-induced structural alterations in the sample. It appears here that image averaging in two dimensions followed by 3D reconstruction (averaging in

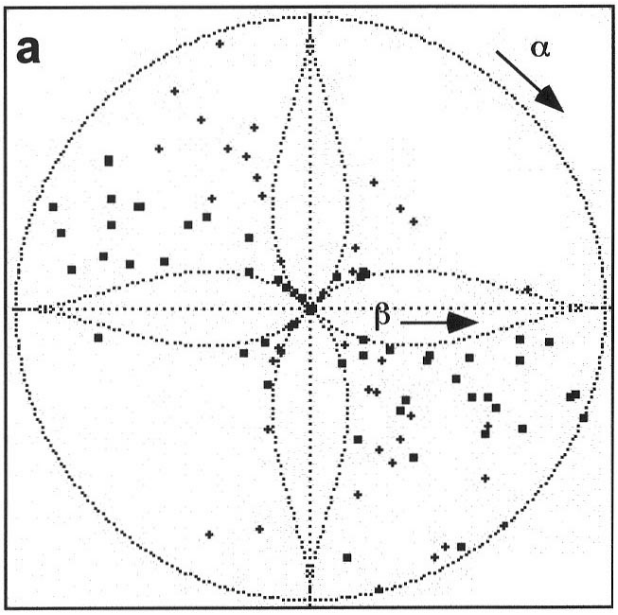

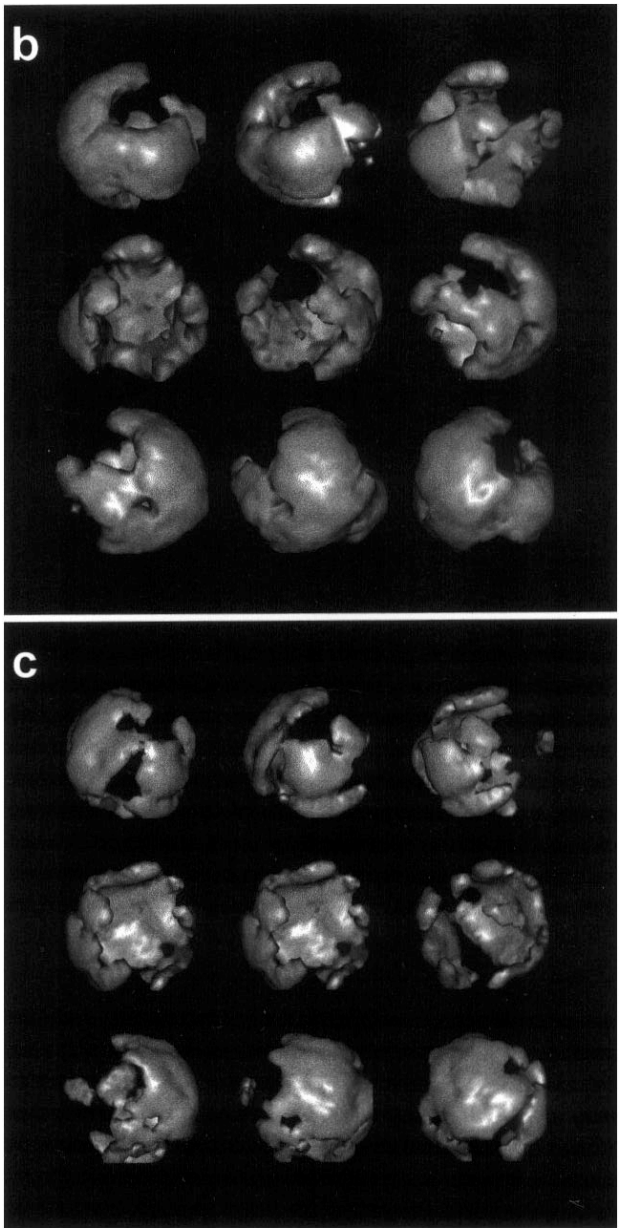

Figure 10. (**a**) Distribution of projection orientations for *E. coli* large ribosomal subunits, and (**b**) *E. coli* large ribosomal subunits, determined by IQAD using the 150 eV loss images. (**b**, **c**). Three-dimensional reconstructions of *E. coli* large ribosomal subunits. Shaded surface representations of reconstructions calculated using the (b) 150 eV loss and (c) NetP images are shown at various density threshold cutoffs. We interpret the higher densities of the NetP signal to be more likely to be real.

three dimensions) would result in a two-fold and excessive blurring of detail. Perhaps it is best simply to proceed to the third dimension directly.

Three-dimensional electron image analysis

The ergodic hypothesis in statistical mechanics can be applied to structural molecular biology: the ensemble of orientational projections of one ribosomal complex is equivalent to the ensemble of projections of many ribosomal complexes lying in different orientations. We next used the farrow-segmented yet aligned 150 eV loss data as direct input to the IQAD (iterative quaternionic angular determination) process. As always, various iterations of this procedure were performed. With a full complement of 300 projections, the reconstructions were difficult to interpret. They were blobby and spherical because of apparent inability of the IQAD procedure to deal accurately with so many images of this nature. We obtained more interpretable results after random splitting of the image population into various smaller subsets of 100 particles each. After numerous reconstructions, we came to a point where we were satisfied that three independent reconstructions, from three non-overlapping subsets of 100 particles each, were yielding essentially the same 3D structure.

The Eulerian angle distributions and 150 eV loss and NetP reconstructions from two of these subsets are shown in Figure 9a for the *E. coli* small ribosomal subunit, and in Figure 10a, for the *E. coli* large ribosomal subunit. In accordance with our interpretation of "rocking" above, the distributions of projection orientations do not form tight, discrete clusters. On the other hand, they are not entirely random either. For example, the Euler angular dispersion for the *E. coli* small ribosomal subunit (Fig. 9a) can be imagined to form a Milky Way-like band, suggesting that it primarily rotates about its long axis.

The Fourier Shell Correlation function yielded reproducible spatial resolution estimates of O(4 nm), at a significance threshold of two standard deviations, between independent 150 eV reconstructions from 100 particles each (see Frank, 1996). Here, we have borrowed the symbol "O(m)" from mathematics, and use it to mean "the order of," or rounded to one significant digit "m." One reason that we have done so is because **no** standard exists for the resolution of electron microscopical reconstructions. Different groups use different measures such as the Fourier Ring/Shell Correlation Functions, or Differential Phase Residual Function, and thresholds of significance are not always stated in publications. It is thus meaningless to quote all digits of, and to compare with each other, the various published resolution measures until some standard is agreed upon. The value of O (4 nm) for our reconstruction here is reasonable and inoffensive given the nature of the data: freeze-dried onto a carbon film, imaged with high electron doses, and of microanalytical quality rather than merely structural. Another reason for using the O(4 nm) terminology is because the reconstructions here do not show much fine detail. We have no easy explanation and consider it better to downplay the importance of digits that are really just **estimates** of resolution. The methodological developments introduced here have yielded a significant improvement over the O(6 nm) resolution of our previous 3D reconstruction (Beniac and Harauz, 1995a). The recent cryoEM reconstructions are much better, of course, at O(2 nm) or O(3 nm) resolution (Frank *et al*., 1995a,b; Frank and Penczek, 1995; Stark *et al*., 1995; Agrawal *et al*., 1996; Lata *et al*., 1996; Verschoor *et al*., 1996).

The molecular weights of the reconstructed subunits can be calculated from their volumes, assuming densities of approximately 0.84 Da/Å^3 for the protein component and 1.03 Da/Å^3 for the nucleic acid component (Stark *et al*., 1995). The results are roughly 886 kDa, for the small subunit, and 1602 kDa for the large subunit, which calculations compare favourably with the accepted values of 930 kDa and 1590 kDa, respectively. However, these values should be viewed with caution since there is a wide range of volumes of ribosomal reconstructions reported in the recent literature (Öfverstedt *et al*., 1994; Frank *et al*., 1995b; Stark *et al*., 1995; Agrawal *et al*., 1996; Lata *et al*., 1996; Verschoor *et al*., 1996). Nonetheless, the exercise of calculating volumes was useful in choosing density thresholds for comparing the corresponding 150 eV loss and NetP reconstructions, from which we conclude below that rRNA reaches the surface of the complex in many places.

Biological correlations

The three-dimensional reconstructions from electron spectroscopic images of the *E. coli* small ribosomal subunit are interpretable and informative (Fig. 9). Although a high density threshold had to be applied before these results appeared meaningful, we had seemingly overcome the limitation of superposition of structural features in two-dimensional projections. We see well-defined head and body domains (roughly one-third:two-thirds in size ratio) in both the 150 eV loss and NetP reconstructions, although the two density distributions are not identical. The 150 eV loss signal comprises also non-specific (i.e., both protein and RNA) mass density. It is thus not reliable to interpret the higher densities in the 150 eV loss reconstruction as corresponding exclusively to rRNA, even though the 150 eV loss image has a stronger signal due to phosphorus than the 100 eV loss image. In Figure 9, from certain perspectives, the canonical "left- and right-lateral" and "quasi-symmetric" or "asymmetric" views seen in negatively-stained preparations (e.g., van Heel and Stöffler-Meilicke, 1985) can be recognised. This consistency with previous EM work of the present reconstructions from electron spectroscopic images is positive and supports the validity of the phosphorus and mass reconstructions. In the small subunit NetP reconstruction at the density threshold in the middle column, there appears to be a channel through the rRNA in the neck region. This feature corresponds directly to a putative passageway for mRNA defined in the gold standard cryoEM reconstructions (Frank *et al*., 1995a,b; Lata *et al*., 1996). The base of the small ribosomal subunit is rRNA-rich, which is an excellent result because this region is deficient in ribosomal proteins (Capel *et al*., 1988). We even see a structure akin to the "spur" or "toe" (Penczek *et al*., 1994; Frank *et al*., 1995a,b; Stark *et al*., 1995) which here is shown to be rRNA. Our results resemble closely even the phosphorus maps defined by low-dose STEM (Boublik *et al*., 1990; Boublik and Wall, 1992).

Similarly, the *E. coli* large subunit reconstructions also agree well with other biological data (Fig. 10) (Svergun *et al*., 1994; Walleczek *et al*., 1988). They are more difficult to interpret than the small subunit reconstructions because they seem more spherical and landmarks such as the three classical protuberances were harder to recognise. The IQAD procedure might have had difficulty determining the correct handedness of these projections. In the large subunit NetP reconstruction, there is a channel in the body of the complex, which can potentially represent the outlet for the nascent polypeptide (Frank *et al*., 1995a,b).

In both subunit reconstructions, the rRNA appears to form a dense central core, reaching the surface in a manner similar to that defined in (Kühlbrandt and Unwin, 1982) by contrast variation using aurothioglucose and glucose embedding. Although some subjectivity was necessarily involved in choosing density thresholds for display of these reconstructions, we used calculated total volumes and relative volumes (see above) to guide us in comparing the 150 eV and NetP results. Thus, the conclusion that rRNA appears to reach the surface was not reached arbitrarily.

Finally, the *Th. lanuginosus* (eukaryotic) small ribosomal subunit reconstructions (not shown) (Harauz and Flannigan, 1992; Beniac *et al*., 1997a) are also meaningful. The eukaryotic small subunit has a prominent bill in the head and basal lobes, in comparison with the prokaryotic small subunit. It has been proposed that the extra non-core rRNA which has been identified by phylogenetic comparison of small ribosomal subunit rRNA secondary structure is deposited in the bill and basal lobe regions of eukaryotic small ribosomal subunits (Brimacombe *et al*., 1990).

To end, the congruence of these various 3D ESI reconstructions with many other independent studies suggests that the former are not thoroughly worthless and possess some degree of validity. We have not created mere RIBosomes {"reconstruction induced blobs" (Baumeister *et al*., 1986)}. Further description of the biological significance of these results needs the use of colour imagery and computer graphics, and hence must be described elsewhere (Beniac *et al*., 1997a,b).

Conclusions

First of all, the nature of high-dose ES images is similar to that of low-dose STEM images: unstained, preferably freeze-dried, high contrast with respect to the background support. The same computational methodology (select, farrow-segment, center in the plane, angular reconstitution) is applicable to both kinds of data. A large number (tens of thousands) of images of different particles is not required here, and is presently a hindrance, since each image is aligned and contributes to the 3D structure directly rather than as part of an averaged cluster. This observation stands in contrast to cryoEM where bigger is opined to be better (Stark *et al*., 1995).

Secondly, these investigations are producing direct information regarding ribosomal rRNA localisation in the ribosomal subunits of *E. coli* and *Th. lanuginosus*. The present *E. coli* results are in favourable agreement with the gold standards derived by cryoTEM. With respect to ribosomes *per se*, many unanswered questions remain in this field, from the structures of eukaryotic (Srivastava *et al*., 1995) or thermophilic (Harauz, 1992; Harauz *et al*., 1992) or unusual rRNAs (Sogin *et al*., 1989) to the issue of eocytes and photocytes (Lake *et al*., 1986). Ribosomology has only just begun a new structural phase, and ESI can contribute via direct RNA mapping as a **complement** to cryoEM of these complexes in single particle analysis, and especially of two-dimensional crystals or other ordered arrays of ribosomal subunits (Aoyama *et al*., 1995; Avila-Sakar *et al*., 1994). In two-dimensional crystals or paracrystals, the ribosomal subunits would thereby present more uniform projection views and enable two-dimensional averaging to higher resolution than is possible with freeze-dried single particles. Moreover, Fourier analysis of such images would provide a more definitive idea of the resolution of the structure retained in electron spectroscopic images.

Finally, at current accelerating voltages, ribosomal subunits present the upper limit of specimen size for ESI, because thicker samples increase the probability of multiple scatter. Viruses, for example, are difficult to study using this technique unless sectioned (e.g., Harauz *et al*., 1995) and cryoEM is clearly the methodology of choice. For very small nucleoprotein specimens (< 10 nm) (e.g., Kyle and Harauz, 1992), however, cryoEM has its limitations because of the low contrast of the technique, and these structures could be better studied by ESI, or STEM/ESI with improved detectors.

Electron spectroscopic imaging and image analysis are not easy. ESI is worth pursuing because it affords direct and complementary information different from bright-field EM of negatively-stained or vitreous ice-embedded specimens. ESI offers elemental microanalysis, and not just dot-mapping, but imaging. Our opinion, based on experimental evidence, is that in spite of the high doses inherent in ESI, and indeed, since they are necessary, because of them, much structural information can be gained on nucleoprotein complexes, with macromolecular selectivity. No other microanalytical technique has been shown to be superior in combining sensitivity, specificity and spatial resolution.

Acknowledgements

The Pfefferkorn Conferences would not be extant were it not for the dedication and industriousness of Dr. Om Johari. The authors are grateful to Mr. Bob Harris (Microbiology, University of Guelph) for assistance with the freeze-drying, and Dr. Robert Starkey (Geology, University of Western Ontario) for the use of and assistance with his Optronics densitometer. FPO was supported by the Medical Research Council of Canada, the National Cancer Institute of Canada, the Protein Engineering Network of Centers of Excellence, the Ontario Cancer Treatment and Research Foundation, and the Natural Sciences and Engineering Research Council of Canada. GH was supported in part by the Natural Sciences and Engineering Research Council of Canada, and by a University of Guelph Research Grant *in lieu* of Salary.

References

Adamson-Sharpe KM, Ottensmeyer, FP (1981) Spatial resolution and detection sensitivity in microanalysis by electron energy loss selected imaging. J Microsc **122**: 309-

314.

Agrawal RK, Penczek P, Grassucci RA, Li Y, Leith A, Nierhaus KH, Frank J (1996) Direct visualization of the A-, P-, and E-site transfer RNAs in the *Escherichia coli* ribosomes. Science **271**: 1000-1002.

Aoyama K, Ogawa K, Kimura Y, Fujiyoshi Y (1995) A method for 2D crystallization of soluble proteins at liquid-liquid interface. Ultramicroscopy **57**: 345-354.

Avila-Sakar AJ, Guan T-L, Arad T, Schmid MF, Loke TW, Yonath A, Piefke J, Franceschi F, Chiu W (1994) Electron cryomicroscopy of *Bacillus stearothermophilus* 50S ribosomal subunits crystallized on phospholipid monolayers. J Mol Biol **239**: 689-697.

Baumeister W, Barth M, Hegerl R, Guckenberger R, Hahn M, Saxton WO (1986) Three-dimensional structure of the regular surface layer (HPI layer) of *Deinococcus radiodurans*. J Mol Biol **187**: 241-253.

Bazett-Jones DP (1993) Empirical basis for phosphorus mapping in DNA: Protein complexes by electron spectroscopic imaging. Microbeam Anal J **2**: 69-79.

Bazett-Jones DP, Ottensmeyer FP (1981) Phosphorus distribution in the nucleosome. Science **211**: 169-170.

Bazett-Jones DP, Locklear L, Rattner J (1988) Electron spectroscopic imaging of DNA. J Ultrastruct Molec Struct Res **99**: 48-58.

Bazett-Jones DP, Mendez E, Czarnota GJ, Ottensmeyer FP, Allfrey VG (1996) Visualization of unfolded nucleosomes associated with transcribing chromatin. Nucleic Acids Res **24**: 321-329.

Beckers ALD, de Bruijn WC, Gelsema ES, Cleton-Soeteman MI, van Eijk HG (1994a) Quantitative electron spectroscopic imaging in bio-medicine: Methods for image acquisition, correction and analysis. J Microsc **174**: 171-182.

Beckers ALD, de Bruijn WC, Jongkind JF, Cleton-Soeteman MI, Apkarian RP, Gelsema ES (1994b) Energy-filtering transmission electron microscopy as a tool for structural and compositional analysis of isolated ferritin particles. Scanning Microsc Suppl **8**: 261-275.

Beckers ALD, Gelsema ES, de Bruijn WC, Cleton-Soeteman MI, van Eijk HG (1996) Quantitative electron spectroscopic imaging in bio-medicine: Evaluation and application. J Microsc **183**: 78-88.

Beniac DR, Harauz G (1993) Visualisation of *E. coli* ribosomal RNA *in situ* by electron spectroscopic imaging and image averaging. Micron **24**: 163-171.

Beniac DR, Harauz G (1995a) Structures of small subunit ribosomal RNAs *in situ* from *Escherichia coli* and *Thermomyces lanuginosus*. Mol Cell Biochem **148**: 165-181.

Beniac DR, Harauz G (1995b) Remarkable moments in single particle electron image analysis. Optik **99**: 62-74.

Beniac DR, Czarnota GJ, Rutherford BL, Ottensmeyer FP, Harauz G (1997a) Three-dimensional architecture of *Thermomyces lanuginosus* small subunit ribosomal RNA. Micron **28**: 13-20.

Beniac DR, Czarnota GJ, Rutherford BL, Ottensmeyer FP, Harauz G (1997b) The *in situ* architecture of *Escherichia coli* ribosomal RNA derived by electron spectroscopic imaging. J Microsc **188**: 24-35.

Beniac DR, Luckevich MD, Czarnota GJ, Tompkins TA, Ridsdale RA, Ottensmeyer FP, Moscarello MA, Harauz G (1997c) Three-dimensional structure of myelin basic protein. I. Reconstruction via angular reconstitution of randomly oriented single particles. J Biol Chem **272**: 4261-4268.

Boublik M, Wall J (1992) Structure of rRNA in the ribosome. In: Proceedings of the 50th Annual Meeting of the Electron Microscopy Society of America. Bailey GW, Bentley J, Small JA (eds.). San Francisco Press, San Francisco, CA. pp. 462-463.

Boublik M, Oostergetel GT, Frankland B, Ottensmeyer FP (1984) Topographical mapping of ribosomal RNAs *in situ* by electron spectroscopic imaging. In: Proceedings of the 42nd Annual Meeting of the Electron Microscopy Society of America. Bailey GW (ed.). San Francisco Press. pp. 690-691.

Boublik M, Mandiyan V, Tumminia S, Hainfeld JF, Wall JS (1990) Structural analysis of ribosomal particles from *Escherichia coli* by scanning transmission electron microscopy. In: Proceedings of the XIIth International Congress for Electron Microscopy. Vol. 3. Peachey LD, Williams DB (eds.). San Francisco Press. pp. 134-135.

Brimacombe R (1995) The structure of ribosomal RNA: A three-dimensional jigsaw puzzle. Euro J Biochem **230**: 365-383.

Brimacombe R, Gruer B, Mitchell P, Osswald M, Rinke-Appel J, Schüler D, Stade K (1990) Three-dimensional structure and function of *Escherichia coli* 16S and 23S rRNA as studied by cross-linking techniques. In: The Ribosome: Structure, Function, and Evolution. Hill WE, Dahlberg A, Garrett RA, Moore PB, Schlessinger D, Warner JR (eds.). American Society for Microbiology, Washington, DC. pp. 93-106.

Capel MS, Kjeldgaard M, Engleman D, Moore P (1988) Positions of S2, S13, S16, S17, S19 and S21 in the 30S ribosomal subunit of *Escherichia coli*. J Mol Biol **200**: 65-87.

Crewe AV (1966) Scanning electron microscopes: Is high resolution possible? Science **154**: 729-738.

Czarnota GJ, Ottensmeyer FP (1996) Structural states of the nucleosome. J Biol Chem **271**: 3677-3683.

Czarnota GJ, Andrews DW, Farrow NA, Ottensmeyer FP (1994) A structure for the signal sequence binding protein SRP54: 3D reconstruction from STEM images of single molecules. J Struct Biol **113**: 35-46.

De Bruijn WC, Sorber CWJ, Gelsema ES, Beckers

ALD, Jongkind JF (1993) Energy-filtering transmission electron microscopy of biological specimens. Scanning Microsc **7**: 693-709.

Egerton RF (1988) A simple parameterization scheme for inner-shell cross sections. In: Proceedings of the 46th Annual Meeting of the Electron Microscopy Society of America. Bailey GW (ed.). San Francisco Press. pp. 532-533.

Engel A, Colliex C (1993) Application of scanning transmission electron microscopy to the study of biological structure. Curr Opin Biotechnol **4**: 403-411.

Engel A, Reichelt R (1988) Processing of quantitative scanning transmission electron micrographs. Scanning Microsc Suppl **2**: 285-293.

Farrow NA, Ottensmeyer FP (1992) *A posteriori* determination of relative projection directions of arbitrarily oriented macromolecules. J Optical Soc Amer A **9**: 1749-1760.

Farrow NA, Ottensmeyer FP (1993) Automatic 3D alignment of projection images of randomly oriented objects. Ultramicroscopy **52**: 141-156.

Frank J (1992) Electron Tomography: Three-dimensional Imaging With the Transmission Electron Microscope. Plenum Press, New York. pp. 1-399.

Frank J (1996) Three-dimensional Electron Microscopy of Macromolecular Assemblies. Academic Press, New York. pp. 1-342.

Frank J, Penczek P (1995) On the correction of the contrast transfer function in biological electron microscopy. Optik **98**: 125-129.

Frank J, Penczek P, Grassucci R, Srivastava S (1991) Three-dimensional reconstruction of the 70S *Escherichia coli* ribosome in ice: The distribution of ribosomal RNA. J Cell Biol **115**: 597-605.

Frank J, Verschoor A, Li Y, Zhu J, Lata RK, Radermacher M, Penczek P, Grassucci R, Agrawal RK, Srivastava S (1995a) A model of the translational apparatus based on a three-dimensional reconstruction of the *Escherichia coli* ribosome. Biochem Cell Biol **73**: 757-765.

Frank J, Zhu J, Penczek P, Li Y, Srivastava S, Verschoor A, Radermacher M, Grassucci R, Lata RK, Agrawal RK (1995b) A model of protein synthesis based on cryo-electron microscopy of the *E. coli* ribosome. Nature **376**: 441-444.

Haider M (1989) Filtered dark-field and pure Z-contrast: Two novel imaging modes in a scanning transmission electron microscope. Ultramicroscopy **28**: 240-247.

Harauz G (1992) Electron microscopical projections of the large ribosomal subunit from *Thermomyces lanuginosus*. Biochim Biophys Acta **1132**: 58-66.

Harauz G, Flannigan DT (1992) Characteristic electron microscopical projections of the small ribosomal subunit from *Thermomyces lanuginosus*. Biochim Biophys Acta **1130**: 289-296.

Harauz G, Ottensmeyer FP (1984) Nucleosome reconstruction *via* phosphorus mapping. Science **226**: 936-940.

Harauz G, van Heel M (1986) Exact filters for general geometry three-dimensional reconstruction. Optik **73**: 146-156.

Harauz G, Stöffler-Meilicke M, van Heel M (1987) Characteristic views of prokaryotic 50S ribosomal subunits. J Molec Evolution **26**: 347-357.

Harauz G, Boekema EJ, van Heel MG (1988) Statistical image analysis of electron micrographs of ribosomal subunits. Methods Enzymol **164**: 35-49.

Harauz G, Letvenuk L, Flannigan DT (1992) Electron image analysis of ribosomal subunits from *Thermus aquaticus*. Biochim Biophys Acta **1129**: 207-214.

Harauz G, Evans DH, Beniac DR, Arsenault AL, Rutherford B, Ottensmeyer FP (1995) Electron spectroscopic imaging of encapsidated DNA in *vaccinia* virus. Can J Microbiol **41**: 889-894.

Harauz G, Cicicopol C, Hegerl R, Cejka Z, Goldie K, Santarius U, Engel A, Baumeister W (1996) Structural studies on the 2.25 MDa homomultimeric phosphoenolpyruvate synthase from *Staphylothermus marinus*. J Struct Biol **116**: 290-301.

Hawkes PW (1980a) Some unsolved problems and promising methods in electron image processing. In: Electron Microscopy at Molecular Dimensions. Baumeister W, Vogell W (eds.). Springer-Verlag, Berlin. pp. 288-299.

Hawkes PW (1980b) The use of moment and other invariants in electron image processing. In: Proceedings of the 7th European Congress of Electron Microscopy. Vol. 1. Brederoo P, de Priester W (eds.). The Seventh European Congress on Electron Microscopy Foundation, Leiden. pp. 500-501.

Heng Y-M, Simon GT, Boublik M, Ottensmeyer FP (1990) Experimental ionization cross-sections of phosphorus and calcium by electron spectroscopic imaging. J Microsc **160**: 161-171.

Knauer V, Hegerl R, Hoppe W (1983) Three-dimensional reconstruction and averaging of 30S ribosomal subunits of *Escherichia coli* from electron micrographs. J Mol Biol **163**: 409-430.

Korn AP (1980) Dark field electron microscopy of the 30S subunit of the *E. coli* ribosome. Ultramicroscopy **5**: 513-520.

Korn AP, Spitnik-Elson P, Elson D (1982) The topology of the 30S ribosomal subunit and a proposal for the surface distribution of its RNA by dark field electron microscopy. J Biol Chem **257**: 7155-7160.

Korn AP, Spitnik-Elson P, Elson D, Ottensmeyer FP (1983) Specific visualization of ribosomal RNA in the intact ribosome by electron spectroscopic imaging. Eur J Cell Biol **31**: 334-340.

Kühlbrandt W, Unwin PNT (1982) Distribution of

RNA and protein in crystalline eukaryotic ribosomes. J Mol Biol **156**: 431-448.

Kyle KM, Harauz G (1992) Electron microscopic visualisation of the 5S rRNA-YL3 complex from *Saccharomyces cerevisiae*. Mol Cell Biochem **117**: 11-21.

Lake JA, Henderson E, Clark MW, Scheinman A, Oakes MI (1986) Mapping evolution with three-dimensional ribosome structure. Systematic Appl Microbiol **7**: 131-136.

Lata RK, Agrawal RK, Penczek P, Grassucci R, Zhu J, Frank J (1996) Three-dimensional reconstruction of the *Escherichia coli* 30S ribosomal subunit in ice. J Mol Biol **262**: 40-52.

McRee DE (1993) Practical Protein Crystallography. Academic Press, San Diego. p. 93.

McWilliams RA, Glitz DG (1991) Localization of a segment of 16S RNA on the surface of the small ribosomal subunit by immune electron microscopy of complementary oligodeoxynucleotides. Biochimie **773**: 911-918.

Moore PB (1988) The ribosome returns. Nature **331**: 223-227.

Mueller F, Döring T, Erdemir T, Greuer B, Jünke N, Osswald M, Rinke-Appel J, Stade K, Thamm S, Brimacombe R (1995) Getting closer to an understanding of the three-dimensional structure of ribosomal RNA. Biochem Cell Biol **73**: 767-773.

Öfverstedt L-G, Zhang K, Tapio S, Skoglund U, Isaksson LA (1994) Starvation *in vivo* for aminoacyl-tRNA increases the spatial separation between the two ribosomal subunits. Cell **79**: 629-638.

Oettl H, Hegerl R, Hoppe W (1983) Three-dimensional reconstruction and averaging of 50S ribosomal subunits of *Escherichia coli* from electron micrographs. J Molec Biol **163**: 431-450.

Ottensmeyer FP (1982) Scattered electrons in microscopy and microanalysis. Science **215**: 461-466.

Ottensmeyer FP (1984) Electron spectroscopic imaging: Parallel energy filtering and microanalysis in the fixed-beam electron microscope. J Ultrastruct Res **88**: 121-134.

Ottensmeyer FP (1986a) Elemental mapping by energy filtration: Advantages, limitations, and compromises. Ann NY Acad Sci **483**: 339-353.

Ottensmeyer FP (1986b) Scattered electrons in biological structure determination. In: Examining the Submicron World. Feder R, MacGowan W (eds.). Plenum, New York. pp. 137-151.

Ottensmeyer FP, Andrew JW (1980) High resolution microanalysis of biological specimens by electron energy loss spectroscopy and by electron spectroscopic imaging. J Ultrastruct Res **72**: 336-348.

Penczek P, Grassucci RA, Frank J (1994) The ribosome at improved resolution: New techniques for merging and orientation refinement in 3D cryo-electron microscopy of biological particles. Ultramicroscopy **53**: 251-270.

Ridsdale RA, Beniac DR, Tompkins TA, Moscarello MA, Harauz G (1997) Three-dimensional structure of myelin basic protein. II. Molecular modelling and considerations of predicted structures in multiple sclerosis. J Biol Chem **272**: 4269-4275.

Schatz M, van Heel M (1990) Invariant classification of molecular views in electron micrographs. Ultramicroscopy **32**: 255-264.

Schatz M, van Heel M (1992) Invariant recognition of molecular projections in vitreous ice preparations. Ultramicroscopy **45**: 15-22.

Shuman H, Chang C-F, Buhle EL Jr, Somlyo AP (1986) Electron energy-loss spectroscopy: Quantitation and imaging. Ann NY Acad Sci **483**: 295-310.

Sogin ML, Gunderson JH, Elwood HJ, Alonso RA, Peattie DA (1989) Phylogenetic meaning of the kingdom concept: An unusual rRNA from *Giardia lamblia*. Science **243**: 75-77.

Srivastava S, Verschoor A, Radermacher M, Grassucci R, Frank J (1995) Three-dimensional reconstruction of mammalian 40S ribosomal subunit embedded in ice. J Mol Biol **245**: 461-466.

Stark H, Mueller F, Orlova EV, Schatz M, Duve P, Erdemir T, Zemlin F, Brimacombe R, van Heel M (1995) The 70S *Escherichia coli* ribosome at 23 Å resolution: Fitting the ribosomal RNA. Structure **3**: 815-821.

Stöffler-Meilicke M, Stöffler G, Odom OW, Zinn A, Kramer G, Hardesty B (1981) Localization of 3' ends of 5S and 23S rRNAs in reconstituted subunits of *Escherichia coli* ribosomes. Proc Natl Acad Sci USA **78**: 5538-5542.

Svergun DI, Pedersen JS, Serdyuk IN, Koch MHJ (1994) Solution scattering from 50S ribosomal subunit resolves inconsistency between electron microscopic models. Proc Natl Acad Sci USA **91**: 11826-11830.

Teague MR (1980) Image analysis via the general theory of moments. J Optical Soc Amer **70**: 920-930.

Tovey NK, Dent DL, Corbett WM, Krinsley DH (1992) Processing multi-spectral scanning electron microscopy images for quantitative microfabric analysis. Scanning Microsc Suppl **6**: 269-282.

van Heel M, Stöffler-Meilicke M (1985) Characteristic views of *E. coli* and *B. stearothermophilus* 30S ribosomal subunits in the electron microscope. EMBO J **4**: 2389-2395.

van Heel M, Schatz M, Orlova E (1992) Correlation functions revisited. Ultramicroscopy **46**: 307-316.

van Heel M, Harauz G, Orlova EV, Schmidt R, Schatz M (1996) The next generation of the IMAGIC image processing system. J Struct Biol **116**: 17-24.

Verschoor A, Frank J, Radermacher M, Wagenknecht T, Boublik M (1984) Three-dimensional reconstruction of the 30S ribosomal subunit from randomly oriented projections. J Molec Biol **178**: 677-698.

Verschoor A, Srivastava S, Grassucci R, Frank J

(1996) Native 3D structure of eukaryotic 80S ribosome: Morphological homology with the *E. coli* 70S ribosome. J Cell Biol **133**: 495-505.

Walleczek J, Schüler D, Stöffler-Meilicke M, Brimacombe R, Stöffler G (1988) A model for the spatial arrangement of the proteins in the large subunit of the *Escherichia coli* ribosome. EMBO J **11**: 3571-3576.

Wallin A, Kübler O (1995) Complete sets of complex Zernike moment invariants and the role of the pseudo-invariants. IEEE Trans Patt Anal Machine Intelligence **17**: 1106-1110.

Discussion with Reviewers

J. Frank: The work in Boublik *et al*. (1984) was not reproducible according to a personal communication by J. Wall, so it was never written up as a paper. Reluctance to accept the findings in the literature is therefore understandable.
Authors: M. Boublik showed lots of crown view, kidney view, etc., NetP distributions. The reason that he did not continue was primarily that he felt uncertain that he could interpret the 110 or 150 eV images unequivocally as crown, kidney, etc., and then relate the NetP distribution to those known views. We do not see that a personal communication from J. Wall, who was not involved with the work, should be involved in this discussion. Nevertheless, almost a decade later, M. Boublik found remarkably similar results using the Z-related high-angle/low-angle signal ratio from scanning transmission electron microscopy of the large subunit (Boublik and Wall, 1992).

J. Frank: Moments are a particularly bad choice of invariants in situations where the surrounding is noisy and the boundary definition uncertain, even after farrow-segmentation.
Authors: This fact was not obvious to us when we began investigating invariant moment functions.

W. de Bruijn: The key question [for the area covered by this paper] is: "Can one image phosphorus in general and in ribosomes in particular by ESI?" In 1984, the answer was yes; currently, the response is maybe, or even definitely no. In my opinion, the authors circumvent this question.
Authors: Electron spectroscopic imaging is of necessity a high-dose technique because it is a microanalytical technique. We have spent a lot of time and effort trying to image phosphorus in nucleosomes and in ribosomes. The doses used were the minimum ones necessary according to the scattering cross-sections for phosphorus as measured by us on image-derived spectra of single virus particles (Heng *et al*., 1990). We think that we succeeded with imaging phosphorus in nucleosomes because our results corresponded to crystallographic results under appropriate preparative conditions (Harauz and Ottensmeyer, 1984; Czarnota and Ottensmeyer, 1996). We believe that we succeeded with imaging phosphorus in ribosomes since our results correspond well with "gold standard" structures derived by cryoTEM (e.g., Frank *et al*., 1995a,b) and with other biophysical studies, and the results make biological sense.

W. de Bruijn: When the material does not tolerate the acquisition of two pre-edge images **in addition to the requested zero-loss image** plus the phosphorus-edge image, phosphorus can not be (adequately) determined in isolated ribosomes (Beckers *et al*., 1994a,b, 1996). Please comment.
Authors: The Beckers *et al*. (1994a,b, 1996) experiments were performed on different instruments and different samples than our work presented here. We have also been frustrated by negative results in detecting phosphorus signals by ESI. With the ribosomal data analysed here, one reason was that the first image scanner that we used was insufficiently accurate to allow detection of the subtle elemental signals. Remarkably different, and positive, results were obtained **from the same negatives** using a better quality (and much more expensive) CCD (charged-coupled device) camera in a colleague's laboratory. The direct digital image acquisition used in the Beckersian experiments is not as sensitive as film to electrons. Specifications of diode arrays in PEELS (parallel-detection electron energy loss microsopy) indicate a sensitivity of 30 electrons per "count" with a noise of three counts (90 electrons), while good CCD cameras require 4-6 electrons per count. The doses required for direct electronic spectral or image acquisition are correspondingly higher than those on film, matched to a minimum magnification and dose in each instance. Since ESI is a **microanalytical** technique, and not just an imaging one, a sufficient number of "counts" is required to detect phosphorus with certainty. The inability of one group to determine phosphorus in ribosomes is not proof of the "impossibility" of the task. The data collection factor is an important one, and probably the prime one to be examined first when looking for explanations for negative results on covalently bound elements at such high local concentrations as in nucleoproteins.

When we started this work *circa* 1989, we were heartened by the results of Bazett-Jones *et al*. (1988), who indicated that they could detect small quantities of DNA despite high radiation doses (which they measured using a Faraday cage), and that different methods of calculation of the elemental signal gave similar results. If the positive results of Bazett-Jones *et al*. (1988) and of our groups were also wrong, in this context, then one has to ask a precise

explanation why from the critics.

W. de Bruijn: Could N. Bonnet's "solution" (published in 1988) have been performed on the existing images?
Authors: There is some confusion between what was published by Bonnet and what was discussed at the meeting. The paper (Bonnet and Liehn, 1988) described the use of a nonparametric statistic (the number of sign changes as an image is scanned row by row) to define when two similar but not identical images (electron micrographs or nuclear medicine scans of an organ) were best aligned with respect to one another (Venot and Leclerc, 1984; Venot *et al*., 1984, 1986). Sometime in the future, **when computer speeds increase significantly**, we shall implement this method for aligning macromolecular images (Frank, 1996) and compare its performance with the presently used (and computationally quicker) correlation function.

During the Pfefferkorn meeting, N. Bonnet suggested that this statistic could be used to define the correction factor (for unequal exposures) of the background image (e.g., 100 eV loss image) before subtracting it from the peak image (i.e., 150 eV loss image) to obtain the elemental signal (Bonnet, 1995), although there would be a small bias in the comparison due to the additional elemental signal. We are grateful to N. Bonnet for his constructive feedback. We shall implement **this** subtraction approach with data that are, at least, accepted as yielding a true elemental map. Furthermore, a comparative analysis of subtraction methods is a major undertaking that goes beyond the scope of the present offering.

W. de Bruijn: Apart from the fact that it is generally accepted that the power law mentioned is not applicable in the phosphorus region [but not forbidden to use, though it has its consequences for the subtracted images (see de Bruijn *et al*., 1993)], extrapolation from one image is unclear to me. Did you use 1 eV channels over that 18 eV slit width and extrapolated from there on? Moreover, it would be helpful to see a truly acquired spectrum integrated over a large ribosomal area (like those in Fig. 2) - this would give the reader a sense of what such an edge is like.
Authors: Unfortunately, we do not have and cannot show an energy loss spectrum over ribosomes. The Zeiss EM902 does not lend itself to a spot analysis over a single ribosome without an inordinately large magnification that would require an equally inordinately large dose. However, the image-derived spectra from single virus particles with similar protein to nucleic acid ratios that were mentioned above (Heng *et al*., 1990) might provide that sense of reality. They were a project and a publication by themselves. The one-parameter correction was arithmetically simple, assuming a constant R over each pixel and calculating A from the power-law equation. We have investigated the quantitative error of one- to four-parameter extrapolation schemes (Ottensmeyer, 1986a,b) and have concluded that for as large a phosphorus signal as that in the ribosome (calculated to be about 20% above the background from the corresponding cross-sections of phosphorus and carbon at 150 eV) a one-parameter fit is quite as accurate as any other.

W. de Bruijn: Because I could hardly find coinciding ribosomes in the 120 eV and 100 eV images in Figure 2, I would prefer to see in an overlay which particles are selected from (a) and (b) and (c) and (d), respectively; now the impression is gained that these two eV images do not belong to the same acquisition frame.
Authors: The images are all 150 eV loss images of large and small ribosomal subunits from the two organisms, one prokaryote and the other eukaryote. The particles shown are all different, and no coincidence should be expected. The point of depicting these structures was to show that they indeed look like ribosomal subunits in terms of their size and shape.

W. de Bruijn: The image segmentation is also a mystery field in relation to the pre-processes applied to the images, like 3x3 median filtering and "interactively" matching ribosomes, followed by the mysterious process of "farrow-segmentation." In a recent paper, Bonnet (1996) reviewed all global and local segmentation processes, emphasising the use of local methods in high resolution images. Would it not be better to omit the median filter and apply local segmentation algorithms? Recently, Beckers *et al*. (1996) have proposed new methods for such localisations. I like to emphasise again, that once ES images show that they can not withstand such tests, phosphorus can not be (adequately) determined in isolated ribosomes. Moreover, the manuscript does not mention aspects of shading correction to be applied. Are they?
Authors: The median filter is a reasonable noise reduction method for these data, and the image segmentation is all local. We stated clearly that local segmentation was superior to global methods, and that local operations implemented here were a positive improvement over those used in our previous studies. Over a local region, the size of a ribosome, shading correction is unnecessary. During the meeting, N.K. Tovey referred me to his earlier Pfefferkorn paper on image segmentation (Tovey *et al*., 1992), in which the methods depicted would certainly be of interest to examine. Comparative studies of segmentation methods are beyond the extent of the present work.

W. de Bruijn: As far as I could deduce, analogue image sets are digitised 1200^2 in a contact mode, using a diaphragm (not aperture) covering an area of 625 μm^2 of the original plates, hence intensities are integrated over an area of 434

nm^2/pixel. How is that value related to the actual area covered by the ribosomes in the original plates taken at 30 K? Or conversely, how many pixels/ribosome are there in the final image after the 2x2 "zoom" before any spectral processing is applied, or what is the pixel area in the final image? In Figure 3, small squares can be seen, sized about 1 nm^2. Is that realistic or "hollow" magnification?

Authors: We believe that "aperture" is the correct English terminology. A straight transliteration of the French word "diaphragme" to give "diaphragm" in English is not appropriate here. The Optronics rotating drum densitometer scanned at a **maximum** resolution of 25 μm per pixel at the film level. Other available settings were 50 μm and 100 μm per pixel. If the negative was recorded at a magnification of 30000x, then each pixel is of dimension 0.833 nm at the object level. Then a 2x2 zoom was performed simply to make the ribosome less "chunky" or pixelated. The final reconstructions were then further magnified by a 2x2x2 zoom to make them more aesthetic (not necessarily more informative); the final displays of the shaded surface views are in Figures 9 and 10. The resolutions of the final reconstructions are **measured** using the Fourier Shell Correlation function.

W. de Bruijn: Although the "farrow-segmentation" procedure has been described before, I would prefer to add to this manuscript a true grey-value frequency histogram of that 64^2 area, illustrating (e.g., subsequently in an overlay) which part of the image information is eliminated by this procedure especially at the margins of the ribosomes and how this area relates to the assumed netP images that in my prints look somewhat smaller.

Authors: It is unclear what information a histogram would convey. Since the farrow-segmentation procedure eliminates high densities near the edge of the image that are non-contiguous with the ribosomal particle, the gray values in the histogram and its overlay would have overlapping gray-values almost anywhere. The procedure is not merely a threshold, but a selection of a contiguous particle-region. The NetP images look smaller than the total mass images because phosphorus is only one component of the structure. The effect of computational farrow-segmentation is akin to that of analogue photographic printing of ribosome images from the negatives at brief exposures and onto high contrast paper (Korn, 1980; Korn *et al*., 1982, 1983).

W. de Bruijn: Though I have not yet read your work (Beniac and Harauz, 1993, 1995a), the solution attributed by Beckers (1994) by enrobing small proteinaceous particles into 1-2 nm thin chromium support films might improve the mentioned aspect about the stability against electron radiation damage.

Authors: We had difficulty making the "single particle analysis" algorithms behave with data of this nature. The same difficulty applies to the more perfect low-dose STEM images (e.g., Engel and Reichelt, 1988; Harauz *et al*., 1996). With the ribosomal subunit ES images here, we tried many different approaches and encountered many dead-ends. But the chromium embedment technique sounds intriguing, albeit, for a different problem than the one with which we had difficulties. If the relative cross-section of the chromium at this thickness in relation to phosphorus is tractable, then this embedment might prove helpful in preserving the ribosomal structure against collapse onto the support film while preparing them for electron microscopy.

M.G. van Heel: How high are the electron doses used in obtaining in your data, and how do these values compare to the typical 10 electrons/$Å^2$ exposures used in vitreous ice microscopy?

Authors: As stated before in this manuscript and many of its predecessors, dose measurements for ESI were published almost a decade ago. Bazett-Jones *et al*. (1988) used a Faraday cage to measure total doses of 2 x 10^5 electrons/nm^2 to form both (**not** each) of the 120 eV and 180 eV loss images in their Zeiss EM902. For comparison, there is a published instance of microanalysis of a virus particle at 10^6 electrons/$Å^2$ (10^8 electrons/nm^2) (Shuman *et al*., 1986). Engel and Colliex (1993) present examples of microanalyses at doses of up to 10^{10} electrons/nm^2. Thus, the electron doses required by this type of **microanalytical** imaging are favourable (often more than one order of magnitude smaller) when compared with **other microanalytical** approaches. A comparison of ESI with purely imaging techniques such as cryoelectron microscopy at 10^3 electrons/nm^2 is misleading. We repeatedly emphasise that the two techniques are complementary.

Additional References

Andrews DW, Ottensmeyer FP (1982) Electron microscopy of the poly-L-lysine alpha helix. Ultramicroscopy **9**: 337-348.

Bonnet N (1995) Processing of images and image series: A tutorial review for chemical microanalysis. Mikrochimica Acta **120**: 195-210.

Bonnet N, Liehn J-C (1988) Image registration in electron microscopy: Application of a robust method. J Electron Microsc Techn **10**: 27-33.

Venot A, Leclerc V (1984) Automated correction of patient motion and gray values prior to subtraction in digitized angiography. IEEE Trans Med Imag **MI-3**: 179-186.

Venot A, Lebruchec J-F, Roucayrol J-C (1984) A new class of similarity measures for robust image registration. Comp Vision, Graphics, Image Proc **28**: 176-184.

Venot A, Liehn J-C, Lebruchec J-F, Roucayrol J-C

(1986) Automated comparison of scintigraphic images. J Nucl Med **27**: 1337-1342.